Article

Modelling the Effects of Aerosol on Mei-Yu Frontal Precipitation and Physical Processes

Yun Zhang [1] [iD]**, Zuhang Wu [1],*, Lifeng Zhang [1],*, Yanqiong Xie [1], Hengchi Lei [2], Hepeng Zheng [1] and Xiaolin Ma [1]**

[1] College of Meteorology and Oceanography, National University of Defense Technology, Nanjing 410073, China; zhangyun.1207@yahoo.com (Y.Z.); xie_yanqiong@163.com (Y.X.); hepeng_z@163.com (H.Z.); xiaolinma@126.com (X.M.)

[2] Institute of Atmospheric Physics, Chinese Academy of Sciences, Beijing 100732, China; leihengchi@sina.com

* Correspondence: zuhangwu666@126.com (Z.W.); zhanglif_qxxy@sina.cn (L.Z.); Tel.: +86-131-1500-6832 (Z.W.)

check for updates

Featured Application: A conceptual model of aerosol-cloud interaction is first built to explain the aerosol effect on Mei-Yu frontal precipitation, with possible application to reducing the significant uncertainties in weather and climate prediction.

Abstract: The Mei-Yu front is a significantly important summer precipitation system in eastern Asia. In recent years, anthropogenic air pollution over the Yangtze-Huaihe region of China has been aggravating continuously. A cloud-resolving model coupled with an idealized frontal model is used to investigate the response of aerosols on the Mei-Yu frontal precipitation. The results indicate that increasing droplet concentrations lead to significant precipitation enhancement with the current pollution levels in Mei-Yu frontal system. Under the polluted conditions, the enhanced cold-cloud process is of great importance. Moreover, with the "towing" of active cold-cloud process, cold-cloud and warm-cloud processes developed mutually. These account for the complicated and special microphysical mechanism for aerosol impacts on Mei-Yu frontal system. Furthermore, two types of "microphysical-dynamic positive feedback loop" caused by the interactions of various physical processes and effects (direct dynamic effect, frontogenesis effect, and vapor pump effect) can be found in the Mei-Yu precipitation, which in turn reinforce the microphysical processes. The combined effect is to increase Mei-Yu front precipitation. The interaction of microphysical processes and dynamic processes, and the positive feedback loops they create are the main physical mechanisms behind the significant impacts of aerosol on Mei-Yu frontal precipitation. This may also be an important feature of climate change in eastern Asia.

Keywords: anthropogenic pollution; climate effect; numerical model; Mei-Yu precipitation; microphysics

1. Introduction

Air pollution has become a global environmental problem, because of its great adverse impact on human health and the climate [1]. China, especially eastern China, has been facing serious environmental issues like the particulate matter (PM) pollution [2], due to the rapidly expanding economic and industrial developments, causing a prominent increase in aerosol loading over this area [3–5].

Aerosols can act as cloud condensation nuclei (CCN) or ice nuclei (IN) and have a significant influence on precipitation through aerosol–cloud interactions (ACI). The aerosol effects have been broadly researched based on data from in-situ measurements [6–11] to spaceborne satellite [12–15].

It has been reported that, given sufficient contact IN due to air pollutions, more ice particles (IP) can be formed, leading to more frequent glaciation of supercooled clouds as the ice crystals grow rapidly at the expense of the droplets in a high ice supersaturated environment, so that more precipitation is produced [16]. On the other hand, if no ice nuclei are present, it is believed that anthropogenic air pollution can suppress precipitation, because high aerosol concentrations increase CCN while reduce cloud particle sizes and lead to a narrow droplet spectrum that inhibits collision-coalescence processes [17–23]. However, other scholars also concluded that aerosols can increase updrafts and cause more precipitation, because increased CCN delay the onset of precipitation and strengthen more freezing of cloud drops as well as associated latent heat release [6,24–29].

Recent investigations showed that the aerosol impacts on precipitation are dependent on meteorological conditions or systems. Under varying meteorological systems, aerosols can have different, or even opposite effects. Tao et al. [30] studied three different deep convection systems (a tropical oceanic squall, a mid-latitude continental squall, and a midafternoon sea breeze convection system) and found that raindrops reach the surface earlier in clean environment, while rainfall is suppressed at early stage in polluted environment. However, in the mature stage, continental storm precipitation decreases, marine storm precipitation increases, and the sea breeze convection precipitation is nearly invariable in polluted environment. Evaporative cooling is the key to the increase/decrease of precipitation in polluted environment. Stronger evaporative cooling results in stronger cold pool, causing more intense convergence and more precipitation. Lynn et al. [31] used the mesoscale model to study deep convection clouds in Florida and found that, compared to clean environments, polluted conditions with mid to high concentrations of CCNs experienced delayed precipitation events, vigorous convection development, and increased peak precipitation rate, but decreased cumulative precipitation. Seifert and Beheng [32] pointed out that as CCN concentration increases, surface precipitation from isolated convective cells decreases, but precipitation from multi-cell convection storms increases. Several scientists have also studied the effect of aerosols on the intensity of tropical cyclones (TC) [33–36]. The studies concluded that pollution aerosols encourage the formation of a large number of cloud droplets, and strengthen the outside convections, but weaken the intensity of the TC. Previous studies focused on the effects of aerosols on clouds and precipitation in mesoscale convective systems (MCS). Recently, scholars turned to examine some synoptic-scale systems, like frontal systems. They found that precipitation reduced slightly near the front but increased farther northward as aerosol concentration was increased [37,38].

To the authors' knowledge, no study has specifically examined the indirect effects of aerosols on the Mei-Yu frontal system, which is the most important system during the summer in eastern China. The Mei-Yu front is a quasi-stationary front stretching for thousands of kilometers, extending eastward from southwestern China to the central Pacific through the Japanese archipelago [39,40]. It is one of the most significant rainfall systems affecting the hydrological cycle in the East Asian monsoon region. Rainstorm associated with Mei-Yu (also called "Baiu" in Japan) is one of the most disastrous weathers in East Asia [41–45]. Research has shown that, over the last few decades, Mei-Yu frontal precipitation in the Yangtze-Huaihe region has been increasing, both in heavy rainfall frequency and in total amount [46–49]. In addition, with the accelerated urbanization and industrialization of the Yangtze River Basin, atmospheric pollution has been on the rise in recent years [50–54]. Measurements have shown that the atmospheric pollution directly contributes to the enhanced concentrations of aerosols in the Yangtze River Basin [55–57]. Have changes in the concentration of aerosols increased or decreased Mei-Yu frontal precipitation? Through what physical processes do aerosols affect Mei-Yu precipitation? These scientific questions have not been studied or revealed yet. To explore the microphysical and dynamical mechanisms of aerosol impacts on Mei-Yu precipitation, numerical experiments based on mesoscale Weather Research Forecasting (WRF) model [58] are implemented. The research could be useful in gaining a better grasp of the effects on weather and climate changes by anthropogenic pollution, and with possible application to reducing the significant uncertainties in weather and climate prediction resulting from such a lack of adequate knowledge.

The rest of this paper proceeds as follows. Section 2 describes the numerical model and the experimental design. Results of the numerical experiments are presented and discussed in Section 3. Section 4 summarizes the physics mechanisms. Finally, conclusions are given in Section 5.

2. Model Description and Experimental Design

2.1. Numerical Framework

In the study, the Advanced Research WRF (ARW) version 3.5 [59] is utilized. To simulate ideal front system, the mode control equations were improved by using Peng et al. [60] method to bring large scale meridional geostrophic wind forces into the momentum equation. We assume that Mei-Yu front is east-west direction and is forced by the meridional geostrophic wind V_g, which is only a function of vertical displacement z. To keep balance, geostrophic potential temperature advection term is introduced in thermodynamic equation, and water vapor advection term is introduced in water vapor equation accordingly. This gives

$$\frac{du}{dt} = -\frac{1}{\rho}\frac{\partial p'}{\partial x} + f(v - V_g) + \mathcal{D}_u \tag{1}$$

$$\frac{dv}{dt} = -\frac{1}{\rho}\frac{\partial p'}{\partial y} - fu + \mathcal{D}_v \tag{2}$$

$$\frac{dw}{dt} = -\frac{1}{\rho}\frac{\partial p'}{\partial z} - g\frac{\rho'}{\rho} + \mathcal{D}_w \tag{3}$$

$$\frac{d\theta}{dt} = S_\theta - u\left(\frac{\partial \theta_g}{\partial x}\right)_{LS} + \mathcal{D}_\theta \tag{4}$$

$$\frac{dq_v}{dt} = S_{q_v} - u\left(\frac{\partial q_{vg}}{\partial x}\right)_{LS} + \mathcal{D}_{q_v} \tag{5}$$

$$\frac{dq_m}{dt} = S_{q_m} + \mathcal{D}_{q_m} \tag{6}$$

$$\frac{d\rho_d}{dt} + \rho_d\left(\frac{\partial u}{\partial x} + \frac{\partial v}{\partial y} + \frac{\partial w}{\partial z}\right) = 0 \tag{7}$$

where u, v, and w are zonal velocity (along the frontal boundary), meridional velocity (perpendicular to the frontal boundary), and vertical velocity in the z direction, respectively. V_g is meridional geostrophic wind velocity, f is Coriolis parameter, θ is the potential temperature of dry air, ρ_d is the density of dry air, D_* expresses the dissipation term of the physical property, q_v is the mixing ratio of water vapor, $q_m = q_c, q_r, q_i, q_s, q_g$ represent the mixing ratio of cloud water, rainwater, cloud ice, snow, and graupel, respectively, $\rho = \rho_d (1 + q_v + q_c + q_r + q_i + q_s + q_g)$ is the total mass density, S_θ represents the heating/cooling effect associated with cloud microphysical processes, S_{q_v} is the source/sink term for water vapor, and S_{q_m} is the source/sink term for hydrometeors. The superscript' represents deviations from the dry, static equilibrium basic-state $\bar{p}(z)$ and $\bar{\rho}(z)$.

The model domain is $L_x = 1000$ km, $L_y = 2000$ km, $L_z = 20$ km in the f plane, using $f = 10^{-4}$ s^{-1}. The lateral boundaries are periodic in x (west-east) and open in y (south-north). The lower boundary is flat without terrain. To inhibit gravity wave reflection from the upper boundary, Rayleigh damping is applied to the vertical velocity in the uppermost 5 km of the domain [61,62]. Horizontal grid resolution is $\Delta x = \Delta y = 5$ km. The number of the vertical levels was 81, with a nearly constant vertical spacing of $\Delta z \approx 250$ m. Time step is $\Delta t = 20$ s. Morrison double-moment cloud microphysics scheme [63] is used and depicted in Section 2.2. Cumulous cloud parameterization is not considered. The radiative effect of clouds is considered, but the direct radiative effect of aerosol is not. The simulations are integrated for 48 h and model output data is available every 5 min.

2.2. Microphysical Scheme

The cloud physics scheme used in this paper follows the two-moment bulk scheme proposed by Morrison et al. [63], but further simplifies the cloud-aerosol interactions by setting cloud droplet number concentrations to reflect changes in aerosol concentration, instead of considering the droplet activation. The scheme takes into account primary production, condensation/evaporation, autoconversion, self-collection, collection between hydrometeor species, melting/freezing, and ice multiplication to describe the warm-cloud and cold-cloud processes in natural rain. However, the aerosol effects on ice nuclei are not included due to the less polluted environment in high levels than near surface. In addition, the saturation adjustment approach is applied to calculate cloud water condensation and evaporation (i.e., excess vapor above water saturation is condensed, or cloud water is evaporated to restore water saturated), with a fixed cloud droplet number concentration. Specifically, if the supersaturation at the advanced time (δ') satisfies $\delta' > 0$, then the condensation rate for cloud droplet (PCD) is computed by Equation (8) as described in the two-moment bulk scheme proposed by Morrison et al. [63]. Instead, if $\delta' < 0$, then the evaporation rate of cloud water is computed by Equation (9), where q_{sw} is the mixing ratio at water saturation, c_p is the specific heat of air at constant pressure and L_v is the latent heat of evaporation. The output of the scheme contains the number concentrations and mixing ratios of four hydrometeor species (rain, cloud ice, snow, and graupel).

$$\text{PCD} = \frac{\delta'}{\Delta t}\left(1 + \frac{L_v^2 q'_{sw}}{c_p r_v T'^2}\right)^{-1} \tag{8}$$

$$\text{PCD} = -\min\left[-\frac{\delta'}{\Delta t}\left(1 + \frac{L_v^2 q'_{sw}}{c_p r_v T'^2}\right)^{-1}, \frac{q'_c}{\Delta t}\right] \tag{9}$$

2.3. Initialization

Initial frontal design is the same as Peng et al. [60]. The design frontal boundary is in the x direction with an initial y-z plane structure as follows:

(i)   Meridional geostrophic wind V_g is:

$$V_g(z) = 3 - 10\tanh(z/7000) \tag{10}$$

(ii)   Initial zonal wind velocity $u_0(y, z)$ is:

$$u_0(y, z) = -\frac{L_y - y}{2y_0} u_m\{1 - \tanh[\beta(L_y - y + \alpha z - y_0)]\} \tag{11}$$

where the assigned parameter values are $u_m = 20\ \text{m s}^{-1}$, $y_0 = 800\ \text{km}$, $\beta = (50\ \text{km})^{-1}$, and $\alpha = 100$.

(iii)   Initial potential temperature $\theta_0(y, z)$ and water vapor mixture ratio $q_{v0}(y, z)$ are broken down into basic-state $\overline{\theta}(z)$ and $\overline{q_v}(z)$ plus disturbances $\theta'_0(y, z)$ and $q'_{v0}(y, z)$ Specifically:

$$\theta_0(y, z) = \overline{\theta}(z) + \theta'_0(y, z) \tag{12}$$

$$q_{v0}(y, z) = \overline{q_v}(z) + q'_{v0}(y, z) \tag{13}$$

The basic-state sounding comes from an average measured distribution over the region [110°–125° E, 28°–32° N], taken from a typical Mei-Yu front weather conditions on 12 July 2010 at 00 UTC. Its convective available potential energy (CAPE) was approximately 1000 J kg^{-1}. Specific parameter values used are the same as Peng et al. [60]. The distributions are shown in Figure 1.
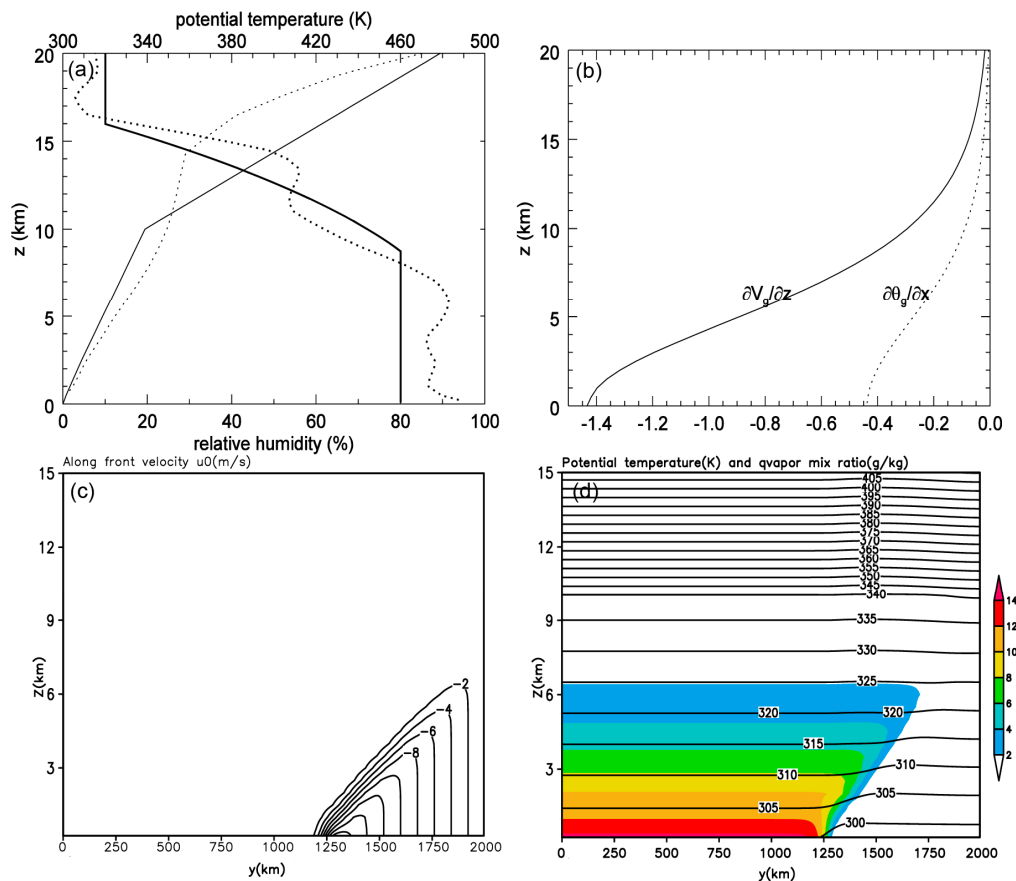
Figure 1. (**a**) Average initial measured (Dotted Line) and ideal model (Solid Line) potential temperature fields plotted together with the basic-state relative humidity field (thin lines are Potential temperature, thick lines are relative humidity) for the region [110°–125° E, 28°–32° N] on 12 July 2010 at 00 UTC. (**b**) Vertical profiles of the vertical shear of the meridional geostrophic wind ($\partial V_g / \partial z$, solid line, Units: 10^{-3} s^{-1}) and the large-scale zonal gradient of the potential temperature ($\partial \theta_g / \partial x$, dotted line, Units: K/100 km). (**c**) Velocity profile along the frontal boundary (u_0, isolines, 2.0 m s^{-1} intervals) and (**d**) potential temperature profile (θ_0, isolines, 5 K intervals) plotted with water vapor mixing ratio (q_{v0}, shaded, 2 g kg^{-1} intervals).

2.4. Experimental Design

With increasing aerosol concentration, the concentration of CCN and hence, cloud droplets, also increase dramatically [64]. Therefore, the concentration of cloud particles can reflect the concentration of aerosol. Given a fixed content of cloud water, the more cloud droplets there are, the smaller the size of droplets could be. For simplicity, cloud–aerosol interactions are not explicitly included in the two-moment bulk scheme described by Morrison et al. [63]; instead, different cloud droplet concentrations are prescribed to imitate the effects of different aerosol concentrations in clean and polluted conditions following some scholars [62,65,66]. For instance, Morrison [61] set the initial cloud droplet concentrations to 250 (750) cm^{-3} to represent the moderately (highly) polluted conditions in understanding the aerosol effect on deep convections. Similarly, this study establishes nine experiments with the initial cloud droplet number concentrations (N_c) set to 50, 100, 250, 500, 1000, 1500, 2500, 3500, and 5000 (cm^{-3}) to reveal the effect of aerosols on Mei-Yu system clouds and precipitation. Note that the highest N_c is set to 5000 cm^{-3} to represent the extreme continental aerosol conditions.

3. Results

3.1. Effects on the Intensity and Distribution of Precipitation

The effect of over-seeding is presented in Weather Modification [67]. Similar results can also be found in our research. Figure 2 shows time series of domain-averaged surface precipitation rate (DPRE). It can be seen in Figure 2a that precipitation begins after t = 14 h in all nine cases. Interestingly, a slight variation of DPRE can be found with the increase of N_c before t = 18 h, but after then, such differences reach amplitude peak at t = 21 h. Note that the changes of DPRE are nonmonotonic with the increase of N_c. More specifically, DPRE increases with N_c ranging from 50 cm^{-3} to 3500 cm^{-3}, but decreases slightly when N_c ranges from 3500 cm^{-3} to 5000 cm^{-3}.
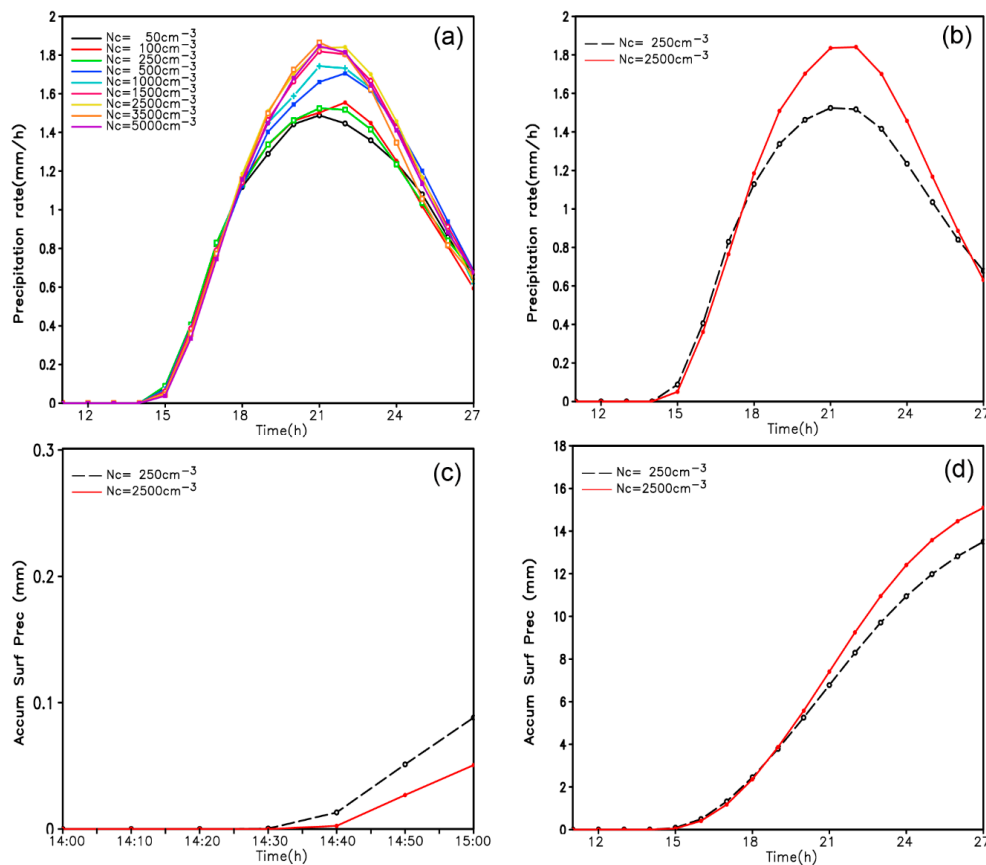

Figure 2. Time series of (**a**) domain-mean surface precipitation rate (mm h^{-1}) in 9 experiments, (**b**) in C-case and P-case only, (**c**) domain-mean accumulated surface precipitation (mm) from t = 14 h to 15 h, and (**d**) domain-mean accumulated surface precipitation before t = 27 h in C-case and P-case.

In order to understand model behavior over a wide range of conditions, we carried out 9 experiments. However, 5000 cm^{-3} is more than in-situ observations in recent, which might occur in the future with much higher urban air pollution. For simplicity, here we focus on two typical conditions, one is typical continent condition case (C-case) and the other is polluted continent condition case (P-case) in Mei-Yu front. Previous observations indicated that droplet concentration is about 100~300 cm^{-3} over continents [68]. Nevertheless, Andreae et al. [69] demonstrated that droplet concentration reaches 2400 cm^{-3} in polluted clouds over the Amazon by observation. Cloud droplet concentration also reaches 1900 cm^{-3} in northern China [70]. Therefore, droplet concentration herein is set to 250 cm^{-3} for C-case, while 2500 cm^{-3} for P-case due to the severe air pollution in Yangtze River basin [54,71]. A similar set was also adopted to investigate the aerosol effects on squall line in Dong et al. [72].

Figure 2b shows time evolution of DPRE in C-case and P-case. Note that precipitation of both cases starts after t = 14 h, but the onset of surface precipitation in C-case (P-case) is at 14:30 (14:40). Precipitation in C-case starts 10 min earlier than P-case (Figure 2c). The effect of aerosol varies in different stages of the precipitation. Before t = 18 h, Precipitation rate is slightly smaller in P-case than C-case, but larger after that, and this phenomenon continues to t = 26 h. The greatest difference is about 22% between P-case and C-case in 21–22 h. Domain-mean accumulated precipitation in the two cases is also quite different after 18:00 (see Figure 2d).

Figure 3 compares the spatial distribution of precipitation in C-case and P-case at three different times. At t = 15 h, the two cases both show a line of precipitation parallel to the front. By t = 18 h, many meso-scale and micro-scale rain cells appear on the frontal rainbands, showing the "core-gape" structure [73] of Mei-Yu front precipitation, but the distribution differences of rainbands are not significant between them. At t = 21 h the differences are clear, the frontal rainband of C-case is more spread-out, while the P-case rainband is closer to the front.
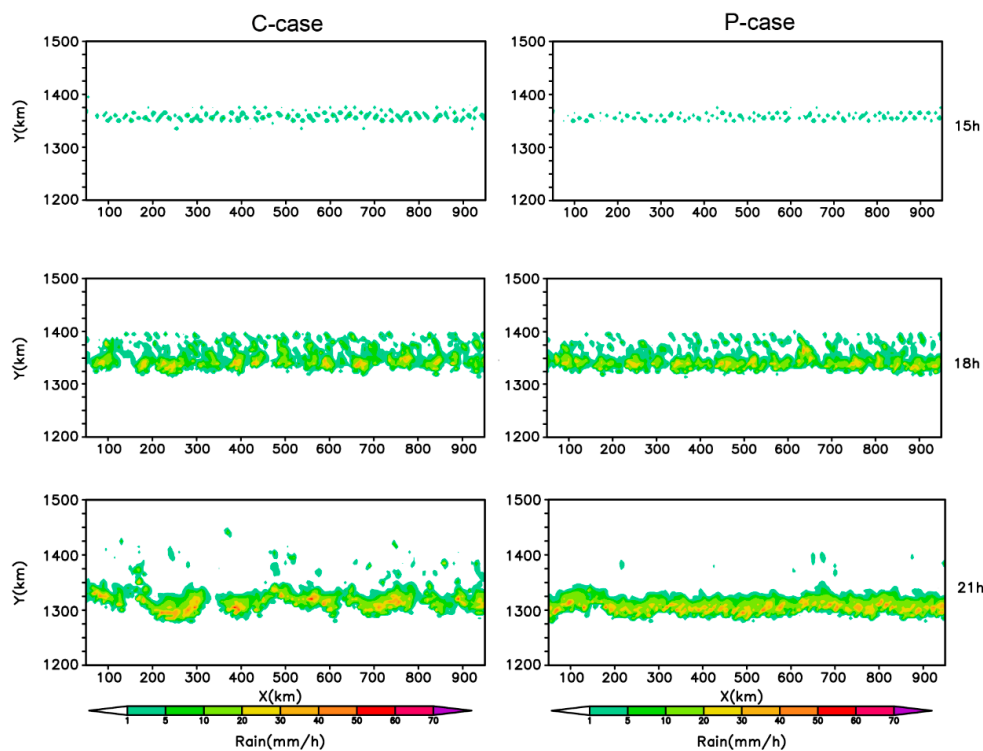

Figure 3. Evolution of precipitation distribution (t = 15, 18, 21 h) in the model domain (Only a 1000 km × 300 km of the domain is presented). The left panels represent C-case, and the right panels represent P-case.

3.2. Effects on Cloud Microphysical Processes

3.2.1. Cloud Microphysical Quantities

At t = 14 h, driven by the Mei-Yu front, cloud water begins to form at a height of 2.5–3 km. The content of cloud water in the two cases is the same, while the number of cloud droplets is higher in P-case, resulting in smaller drop size. At t = 14 h 30 min, surface precipitation begins to appear in C-case. Figure 4 shows the average vertical distribution profile of hydrometeors in the two cases, where Q_c, Q_r, Q_i, Q_s, and Q_g represent the mixing ratios of cloud water, rain water, ice crystals, snow, and graupel, respectively. It is notable that, at this time, the two cases contain only cloud water and rain water. Q_c of P-case is greater than that of C-case, but Q_r is less obvious (Figure 4a,b). This indicates that cloud drop-size of P-case is smaller, and less efficient at forming stage of raindrops. Figure 2c shows surface precipitation starts at t = 14 h 40 min in P-case, 10 min later than that of C-case.
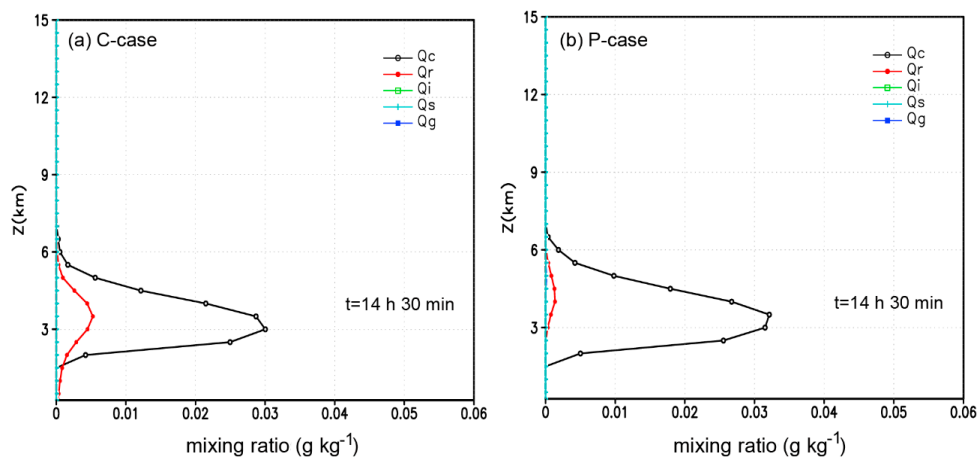
Figure 4. Vertical profiles of domain-averaged mixing ratios (g kg^{-1}) of hydrometeors for (**a**) C-case and (**b**) P-case at t = 14 h 30 min. The symbols Q_c, Q_r, Q_i, Q_s, and Q_g represent the mixing ratios of cloud water, rain water, ice crystals, snow, and graupel, respectively.

In the early stage of precipitation (t = 15 h), cloud top extends to a height of 8 km (0 °C layer located at 3.75 km height) and ice phase process starts. Even though there is smaller Q_r in P-case than in C-case, P-case has larger Q_s and Q_g (see Figure 5a,b). Overall, P-case has less warm-cloud hydrometeors and more cold-cloud hydrometeors than C-case (Figure 5c).
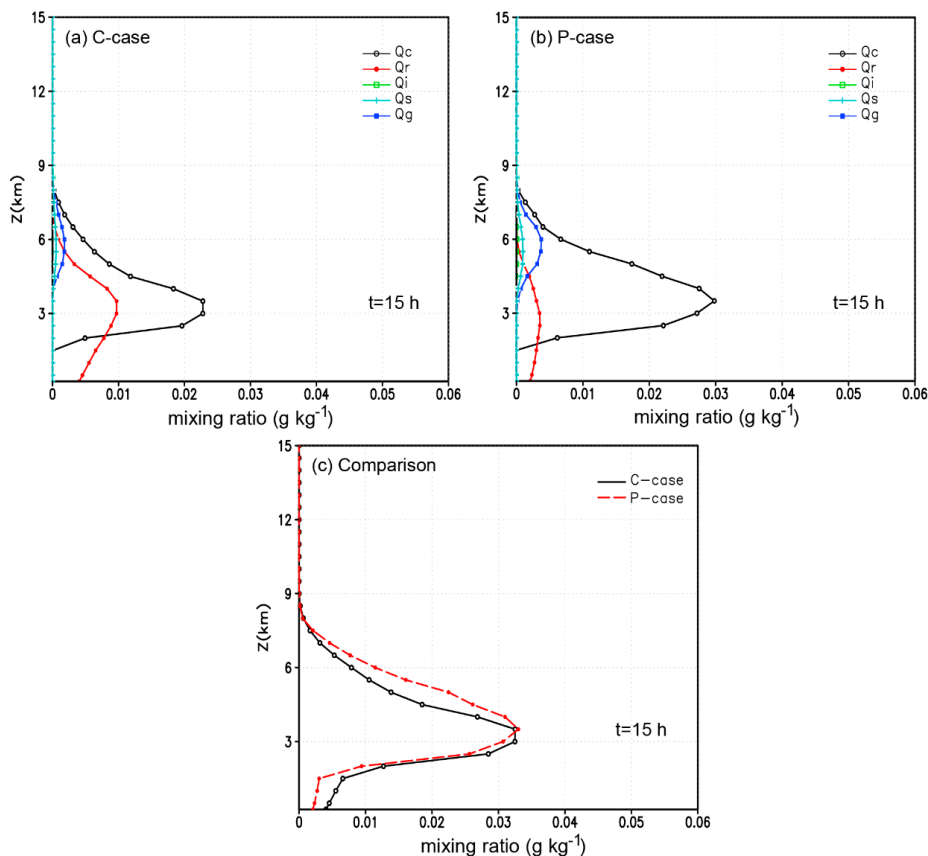

Figure 5. Vertical profiles of domain-averaged mixing ratios (g kg^{-1}) of hydrometeors at t = 15 h (**a**) C-case, (**b**) P-case, (**c**) Vertical Profile of Total Hydrometeors in two cases. The symbols Q_c, Q_r, Q_i, Q_s, and Q_g represent the mixing ratios of cloud water, rain water, ice crystals, snow, and graupel, respectively.

More cloud droplets with smaller drop-size in P-case suppress the conversion of cloud droplets to raindrops, which inhibits precipitation in the early stage, and, meanwhile, leads to more cloud water detained and foster more snow and graupel formation at upper levels. These two aspects are the main differences in cloud physical characteristics of two cases at the onset of precipitation.

In the developing stage of precipitation (t = 18 h), rain water content exceeds cloud water below a height of 3 km. Snow and graupel content increase dramatically in both cases above a height of 3 km (Figure 6a,b). This shows that cold rain processes are greatly invigorated in the developing stage. Comparing the two cases, the content of rain water is quite similar, but P-case has more hydrometeors of all other species, and larger content of total hydrometeor. The biggest difference is at a height of 6 km (Figure 6c). Note that, in addition to increased ice-phase hydrometeors, the content of cloud water in P-case is much greater now than that at t = 15 h, implying that the condensation process (warm-cloud process) has also been invigorated.
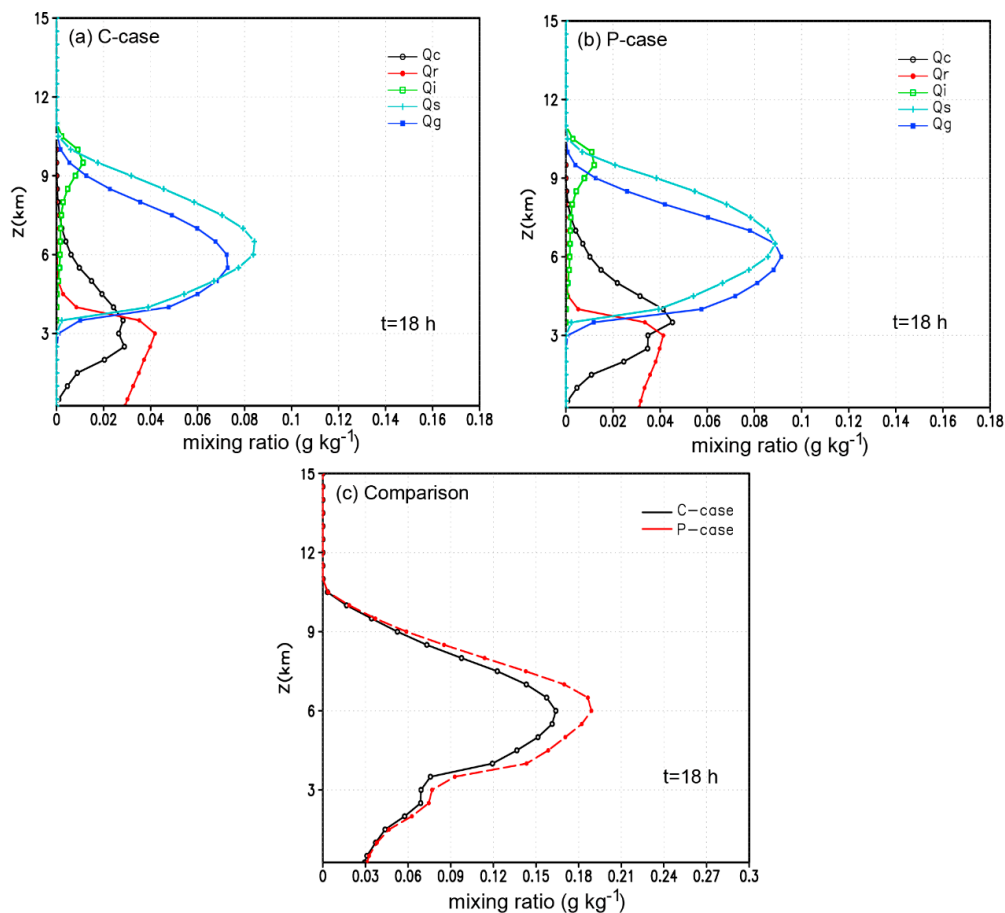

Figure 6. Same as Figure 5, but for t = 18 h.

In the maximum precipitation period (t = 21 h), ice-phase hydrometeor content of both cases grows dramatically. The two most prominent types of hydrometeors are still snow and graupel (Figure 7). Figure 8 shows the average zonal vertical distribution of hydrometeors content at t = 21 h. Comparing the two cases, the difference in hydrometeor content is greatest in the mixed-phase layer (0 °C to −20 °C). The difference is mainly in the graupel, snow, and cloud water content. In P-case, maximum hydrometeor mixing ratios are 2 g kg^{-1} for graupel; 1.5 for snow crystals; and 0.5 for cloud water, which are 2 times, 1.5 times, and 1.7 times of those in C-case, respectively. The content of surface rain water in P-case is roughly double than C-case (Figure 8c,d). Correspondingly, the greatest difference of DPRE (about 22%) appears at this time between the two cases (Figure 2c).
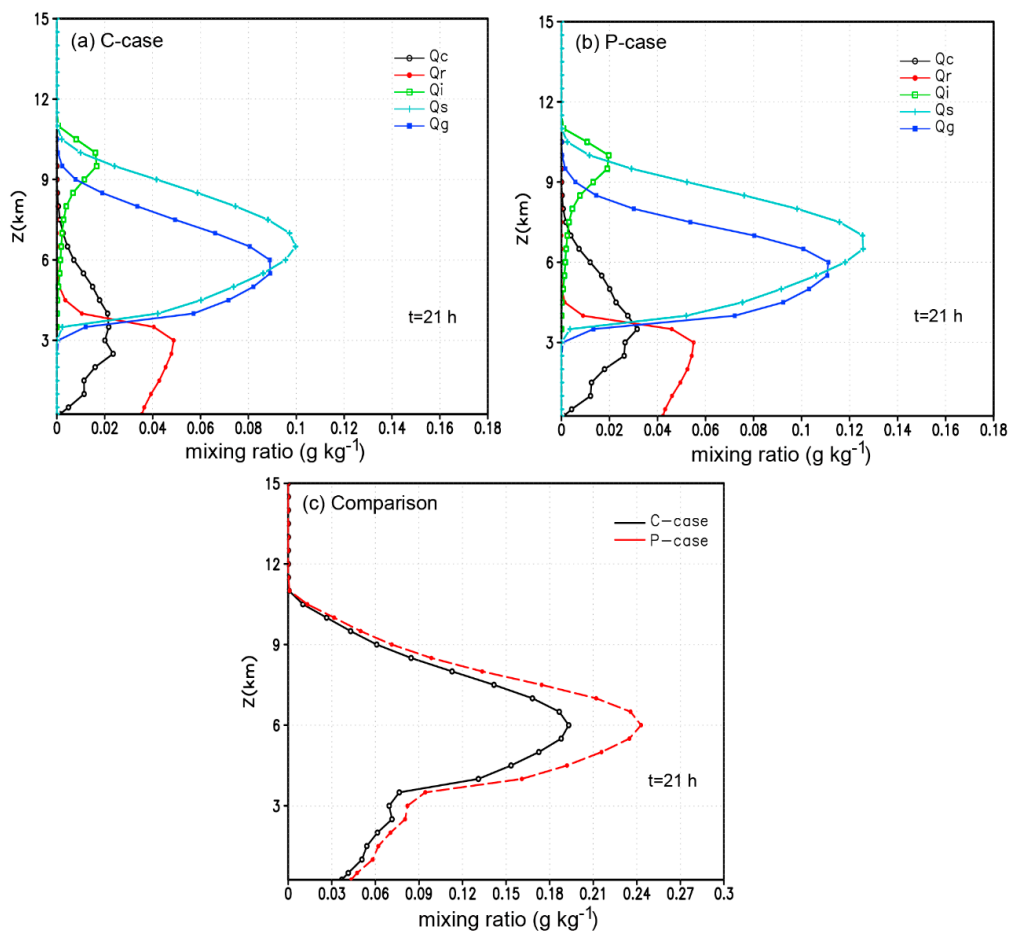
Figure 7. Same as Figure 5, but for t = 21 h.

Overall, the main differences appear in the mixed-phase layer at a height of 6 km, where snow and graupel grow rapidly [74,75]. This suggests that aerosol concentration influences the amounts of cloud water above the 0 °C isotherm, and then influences the production and amounts of graupel and snow in mixed phase layer, thereby affecting the formation and amounts of precipitation in Mei-Yu system.
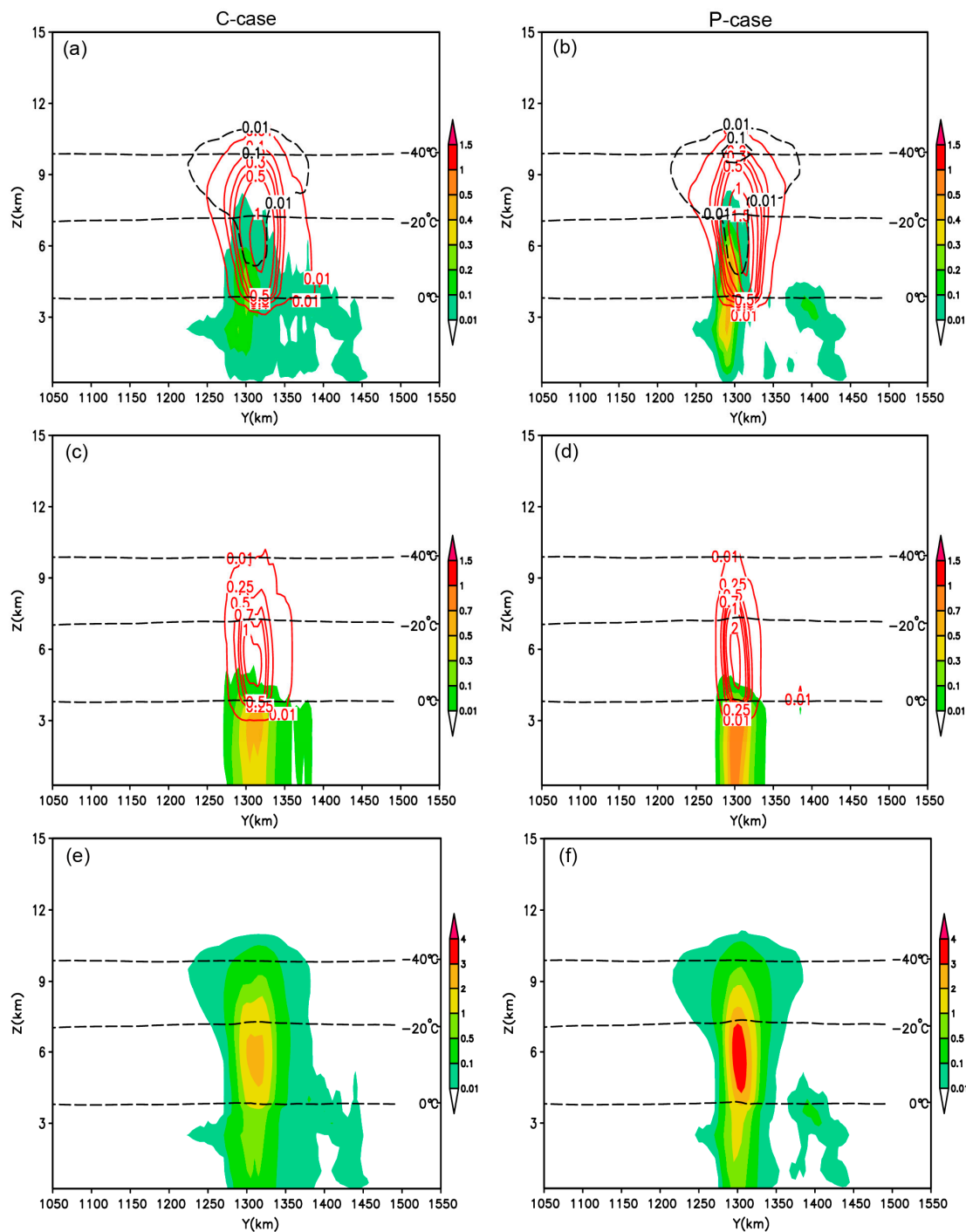
Figure 8. Vertical cross sections of zonal-mean mixing ratios (g kg^{-1}) of hydrometeors at t = 21 h (**a**,**b**) cloud water (shadow), ice crystals (black dashed line), snow (red solid line);(**c**,**d**) rain water (shadow) and graupel (red solid line);(**e**,**f**) the total hydrometeors contents (shadow). Only a 500 km × 15 km of the domain is presented. The left panels show C-case, the right panels show P-case.

3.2.2. Cloud Microphysical Processes

The differences in precipitation and hydrometeor content caused by aerosols are closely related to microphysical processes. In order to better understand the microphysical differences, we analyze the various sources (sinks) of precipitable hydrometers in both cases. Tables 1–3 give the sources (sinks) of the main precipitable hydrometeors (rain water, graupel, and snow), as well as their associated conversion rates during the onset of precipitation period and the peak precipitation period.

Microphysical Processes of Rain Formation

During the early stage of precipitation (t = 15 h), the formation of rain water mainly comes from collision-coalescence between raindrops and cloud droplets. The second significant sources of rain water at this time include the melting of snow and graupel (see Table 1). Noted that auto-conversion of cloud droplets into raindrops is very important in the initial formation of raindrops, even though it occurs with a very low efficiency. The concentration of cloud droplets in C-case is lower. Accordingly, their size is larger, and they are more efficient at auto-converting into raindrops than in P-case. In fact, the maximum rate of auto-conversion of cloud droplets into raindrops is 25 times in C-case than in P-case (see Table 1). Therefore, raindrops form earlier; then grow larger by collision coalescence and fall faster in C-case, leading to the rainfall to surface earlier (Figure 2c,d). By contrast, the formation of raindrops in P-case is inhibited in the initial stage of the precipitation, due to the initial concentration of cloud droplets is relatively higher and cloud drop-size is smaller. Furthermore, low conversion rate means more retention of cloud water, which will be transported to higher levels by frontal updraft, leading to enhancement of cold-cloud process.

During the maximum precipitation period (t = 21 h), conversion rates of both cases have increased dramatically, and the largest conversion rate is the melting of graupel. At this time, except for the auto-conversion of cloud water into rain, all the other rainfall source items (conversion rates) in P-case is greater than in C-case. The ratios of the maximum conversion rate are as follows: the melting rate of graupel melting is about 2 times; melting rate of snow is 1.3 times; and the collection rate of cloud water by rain is 1.8 times. These results show that cold-rain processes enhance greatly under the polluted conditions.

It is noted that evaporation of raindrops also strongly increases in the maximum precipitation period. Raindrop evaporation in P-case is twice stronger than C-case. By the above analysis, it can be inferred that cold-rain processes play a key role in precipitation enhancement during the maximum precipitation period, especially the melting of graupel and snow. Therefore, it is important to study the formation of graupel and snow, which helps understand the impacts of aerosol on precipitation formation mechanism.

Table 1. Source-sink terms of rain (after Morrison and Pinto [76]) and maximum conversion rates in its microphysical processes (10^{-3} g kg^{-1} s^{-1}).

Process	Description	15 h		21 h	
		C-Case	**P-Case**	**C-Case**	**P-Case**
PRA	Accretion of droplets by rain	0.7	0.4	1	1.8
PRC	Auto-conversion of droplets to form rain	0.0016	6×10^{-5}	0.0012	5×10^{-5}
PSMLT	Melting of snow to form rain	0.027	0.033	2.7	3.5
PGMLT	Melting of graupel to form rain	0.05	0.09	4.5	8
PRACS	Collection of rain-snow to form rain	0.0057	0.0087	0.18	0.25
PRACG	Collection of rain-graupel to form rain	0.0045	0.0017	0.5	0.8
PRE	Evaporation of rain	−0.05	−0.03	−0.33	−0.6

Microphysical Processes of Graupel Formation

Melting of graupel is the most important source of rain formation. Table 2 lists the various microphysical process of graupel formation. It can be seen in the table that during the early stage of precipitation, the most significant physical processes of graupel formation are: Accretion of cloud droplets by graupel to form graupel, deposition of graupel, and collection of cloud droplets by snow to form graupel.

During the maximum precipitation period, the production rate of graupel enhanced greatly due to increased upward movement in cold-cloud, as well as the presence of large amounts of supercooled water droplets. The collections of supercooled cloud droplets and raindrops by graupel are two of the biggest source items in the growth process of graupel. The followed important source items are the deposition of graupel, ice-rain collection to graupel, collection of cloud droplets by snow to form

graupel, and collection of snow by super-cooled raindrop to form graupel. By contrast, during the early stage of precipitation, P-case has more super-cooled cloud water than C-case (see Figure 4), which contributes to the growth of snow and graupel through riming. In addition, Graupel also grows through the Wagner–Bergeron–Findeisen (WBF) process. These processes cause larger content of graupel in P-case than C-case (see Figure 4). During the maximum precipitation period in P-case, super-cooled cloud droplets are the main participants in forming graupel through accretion growth.

Table 2. Same as Table 1, but for graupel.

Process	Description	15 h		21 h	
		C-Case	P-Case	C-Case	P-Case
PSACWG	Accretion of cloud droplets by graupel to form graupel	0.39	0.66	0.8	2
PRACG	Collection of raindrops by graupel to form graupel	0.043	0.033	0.6	1.1
PRDG	Deposition of graupel	0.089	0.14	0.27	0.55
PSACR	Collection of snow by super-cooled raindrop to form graupel	0.025	0.04	0.14	0.22
PGSACW	Collection of cloud droplets by snow to form graupel	0.12	0.14	0.12	0.33
PIACR	Ice-rain Collection to graupel	0.09	0.04	0.24	0.5
PGRACS	Collection of raindrops by snow to form graupel	0.0003	0.0028	0.024	0.035
MNUCCR	Freezing of raindrop to form graupel	0.013	0.0008	0.01	0.0033

Microphysical Processes of Snow Formation

In addition to graupel's important contribution to the formation of precipitation, snow also plays an important role. Table 3 lists the various microphysical processes that can form snow, and their associated conversion rates (10^{-3} g kg^{-1} s^{-1}). During the initial precipitation stage, there are three major processes involved in the growth of snow. They are: the collection of rain-snow to form snow; accretion of super-cooled cloud droplets by snow (both called riming); and deposition of snow crystals. Of these, riming with super-cooled raindrops is of greatest significance. Comparing the conversion rate in two cases, there is more snow riming growth in P-case (0.047) than in C-case (0.036). This is related to the increased amount of cloud water in the mixed-phase region (approximately 4–7 km above the surface).

It is noted that, during the maximum precipitation period, snow growth by deposition has become the largest contributor to snow formation. Riming with super-cooled rain and cloud droplets are second and third respectively. This is perhaps related to two things: increased evaporation of cloud droplets; and increased water vapor transported to higher altitudes by enhanced frontal updrafts in the high humidity environment of the Mei-Yu front. Comparing the two cases, the maximum rate of snow production in all of the above processes is greater in P-case than in C-case. Hence, there is much more snowfall under polluted conditions. This is mainly because the P-case has more supercooled cloud water and rain water to foster the formation of snow.

Table 3. Same as Table 1, but for snow.

Process	Description	15 h		21 h	
		C-Case	P-Case	C-Case	P-Case
PRACS	Collection of rain-snow to form snow	0.0545	0.0715	0.24	0.35
PSACWS	Accretion of super-cooled cloud droplets by snow (snow riming)	0.036	0.047	0.16	0.24
PRDS	Deposition of snow	0.016	0.0083	0.45	0.65
PRAI	Auto-conversion of ice to form snow	0.0043	0.0048	0.014	0.024
PRCI	Collection of ice crystals by snow	0.011	0.001	0.013	0.024
PRACIS	Accretion of ice by rain to form snow	0.0001	1.3E-5	5E-05	2E-05

By analyzing the physical processes behind the formation of the main precipitable hydrometeors under different pollution conditions, we can see that raindrops mainly come from the melting behavior of graupel and snow during the maximum precipitation period. The primary growth mechanisms of

graupel and snow are riming and deposition. In high-polluted environment, cold-cloud processes are more pronounced, producing more ice particles, which then melt and produce more raindrops. The invigoration of cold-rain processes in a polluted environment is the main microphysical mechanism behind increased Mei-Yu system rainfall production.

Compared with previous studies about frontal systems and severe convective systems, there are some similar results. Increased aerosols generally lead to smaller cloud particle sizes, suppress collision–coalescence process, hinder the warm-rain processes and hence delay rain-drop formation. Meanwhile, there is higher liquid water content (LWC) above the freezing level [30,77,78]. However, there are some differences in these systems. For deep convective system, the retention of higher LWC above the freezing level enhances riming process and suppresses deposition process, leading to precipitation enhancement. For frontal system, the deposition process is enhanced but riming is suppressed, causing precipitation decrease in high aerosol concentration environments [37,79]. Note that both riming and deposition processes are enhanced in Mei-Yu frontal system, especially in developing and vigorous periods.

This may be due to two contributors: one is that more cloud water is transported to high levels where it evaporates and is deposited onto ice particles (WBF process); the other is that the invigorated cold-cloud process releases more latent heat, strengthens updrafts to increase the vertical transportation of water vapor. This would increase the degree of water vapor super-saturation to ice at high levels and speed up the growth of ice-phase particles by deposition.
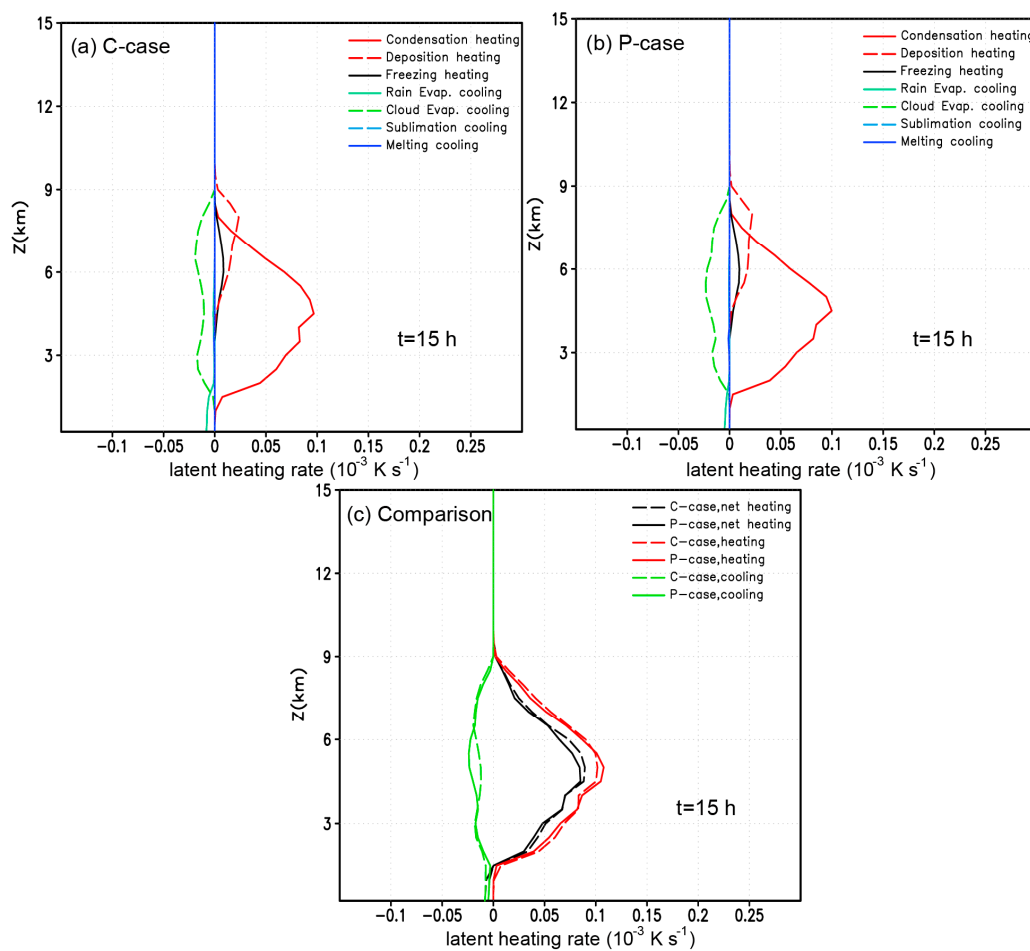

Figure 9. Vertical profiles of domain-averaged latent heating at t = 15 h (Units: 10^{-3} K s^{-1}) (**a**,**b**) latent heating rates of individual processes (left panel shows C-case, right panel shows P-case), (**c**) total latent heating (heating by condensation, freezing and deposition; cooling due to sublimation, melting and evaporation; net heating is the sum of heating and cooling).

3.3. Effects on Latent Heat

Varying aerosol concentrations affect the content and vertical distributions of hydrometeors, which inevitably brings in different latent heat. Latent heating includes three parts: condensation heating; freezing heating; and deposition heating. Likewise, latent cooling includes evaporation cooling, melting cooling, and sublimation cooling. Figure 9 shows an average vertical profile of latent heating during the early stage of precipitation. It can be seen that the largest source of heating is condensation heating. Secondary sources are deposition heating, and freezing heating. The biggest source of cooling is the evaporation of cloud droplets (Figure 9a,b).

Comparing the two cases, there are only a few differences during the initial stage of precipitation (Figure 9c). At a height of 6 km, the evaporative cooling of cloud water is slightly larger in P-case than in C-case. Correspondingly, deposition heating is slightly larger in P-case than in C-case. This indicates that the higher cloud water content with smaller cloud droplets at high levels in P-case results in more evaporation, leading to the enhanced deposition process to produce ice-phase particles. That is to say, the WBF conversion proceeds faster with the polluted conditions. In addition, at a height of about 6 km in P-case, the freezing heating is a bit higher than that in C-case. This is mainly due to the more cloud droplets with smaller size in P-case being carried to higher levels (Figures 4 and 5), where they either freeze, or are accreted by ice-phase particles, releasing more latent heat (Figure 9a,b). It is noted that increased latent heating due to freezing and deposition creates a "warmer bed" for cold-cloud development in P-case.
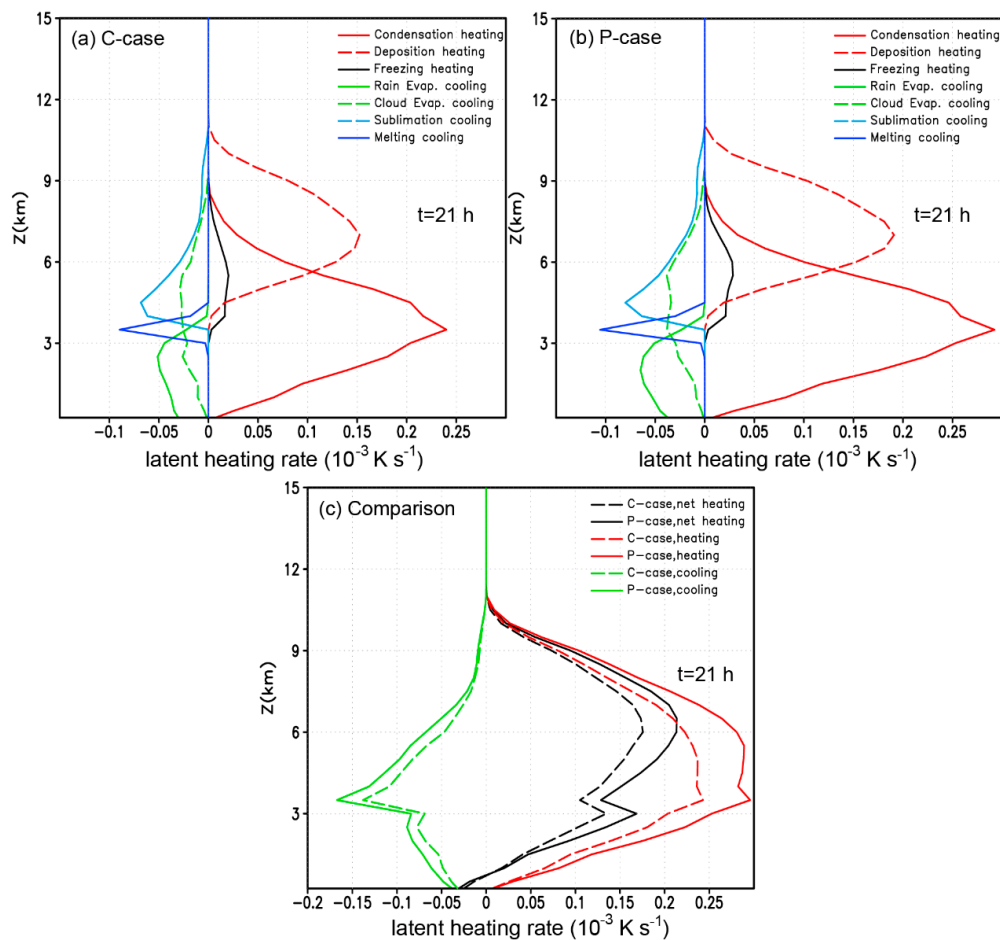

Figure 10. Same as Figure 9, but for t = 21 h.

As the cloud system develops and cold-cloud processes strengthen, P-case ice-phase particles release more and more latent heat from freezing and deposition. By t = 16 h, P-case latent heating has

already approached C-case latent heating (not shown); At t = 17 h, the warm-cloud latent heat profiles are similar, but cold-cloud heating in P-case is clearly stronger than in C-case (not shown). From here, a shift occurs, and P-case net latent heating begins to exceed C-case.

Figure 10 gives the vertical profile of the average latent heating rate in the model domain during the maximum precipitation stage (t = 21 h). Both heating (due to condensation, deposition, and freezing) and cooling (due to sublimation, melting, and evaporation) increase dramatically in the two cases (Figure 10a,b). The height of the net latent heating maximum value has moved up to over 6 km (Figure 10c). This indicates that latent heating in cold-cloud processes increased markedly with the development of the precipitation system. Comparing the two cases, not only freezing and deposition heating, but also condensation heating are larger in P-case. This suggested that P-case water vapor content may already be greater than C-case. Meanwhile, evaporation, melting, and cooling in P-case are all greater than in C-case.

4. The Dynamic Effects

Tao et al. [78] summarized a great deal of the recent researches regarding the impact of aerosols on convective clouds and precipitation and pointed out that aerosols impact clouds and precipitation by two dynamic mechanisms. The first mechanism is stronger updrafts/downdrafts resulting from enhanced latent heat release. The second mechanism is stronger convergence due to stronger evaporative cooling. These results were mostly derived from researching strong convective systems. Is there a difference between the physical mechanisms pointed out by Tao et al. [78] and those at work in the Mei-Yu frontal system? How do the various physical processes or mechanisms work together? Those questions motivate us to do more research.

4.1. Direct Dynamic Effect

The variations of aerosol concentration result in differences in microphysical processes, leading to differences in latent heating and cooling. The vertical cross sections of zonal-mean latent heat and cross-front wind perturbation vectors (v', w) (here, $v' = v - V_g$) are shown in Figure 11. At t = 21 h, the main heating region is located in the ascent region of frontal zones and the main cooling region is located in the descent region of frontal zones. Compared to C-case, P-case heating and cooling are both much greater. In P-case, heating reaches 18 K h^{-1} and cooling reaches −6 K h^{-1}, which is 2–3 times larger than C-case. Strong heating invigorates updrafts, while strong cooling invigorates downdrafts, causing both stronger updraft and downdraft in P-case than in C-case (Figure 11). At the same time, P-case convergence in the low-level frontal region and divergence at high altitudes are both greater than C-case (Figure 12).

Based on the above analyses, under polluted conditions, a large number of small droplets are transported to high levels by frontal updraft, leading to the enhanced riming and WBF processes to produce more ice-phase droplets, which increases latent heat release. As a result, the extra heat reinforces the updrafts and thus enhances cold-cloud processes, leading to the formation of large amount of snow and graupel. On the other hand, with large amounts of snow and graupel falling and melting, rain water content increases below the frontal zone, leading to more evaporation. Stronger melting and evaporation cooling produce a stronger cold pool and strengthens downdrafts, resulting in stronger low-level convergence under the action of frontal wind shear.

Here, the roles of latent heat (strengthens updrafts, downdrafts, and low-level convergence) under polluted conditions involves two mechanisms pointed out by Tao et al. [78], which are the latent heat–dynamic effect and the cool pool effect. We suggest that the two direct effects driven by latent heat release may be collectively referred to as the first dynamic effect/direct dynamic effect (DDE).
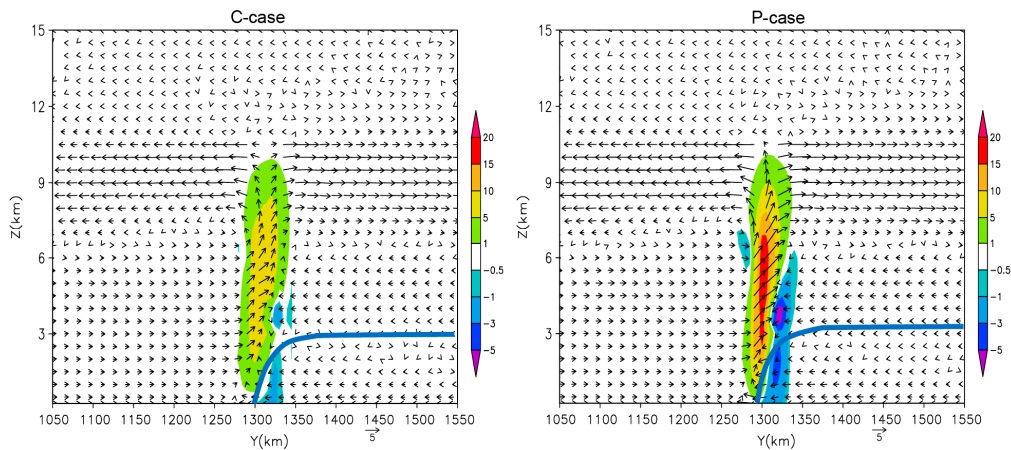
Figure 11. Vertical cross sections of zonal-mean Latent Heating (The warm color shadings show heating greater than $1 \, \mathrm{K} \, \mathrm{h}^{-1}$; the cold color shadings show cooling less than $-0.5 \, \mathrm{K} \, \mathrm{h}^{-1}$) and cross-front wind perturbation vectors (v', w) at t = 21 h. The blue thick line indicates the front. Only a 500 km × 15 km of the domain is presented. The left panel shows C-case, the right panel shows P-case.
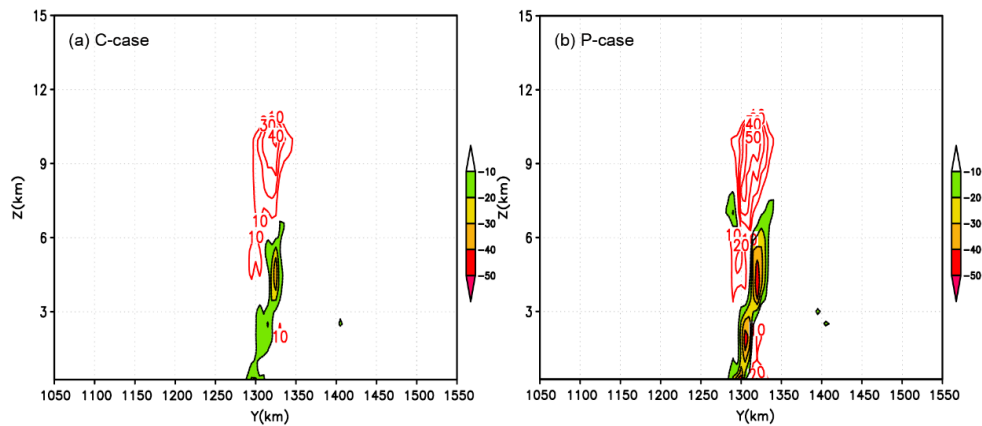

Figure 12. Vertical cross sections of zonal-mean Divergence at t = 21 h (The contours show divergence greater than $10^{-5} \, \mathrm{s}^{-1}$, the color shadings show convergence less than $10^{-5} \, \mathrm{s}^{-1}$). Only a 500 km × 15 km of the domain is presented. The left panel shows C-case, the right panel shows P-case.

4.2. Frontogenesis Dynamic Effect

4.2.1. Impacts on Frontogenesis

Significant effects of aerosols on cloud microphysics and dynamics of MCSs have been found [25,30,77]. For the Mei-Yu front, a synoptic-scale system, whether or not, and how, did aerosols associated with thermodynamic and dynamic effects influence the frontal structure and intensity, have not been studied yet.

A significant character of Mei-Yu front is strong humidity gradient across the front. Therefore, it is more suitable to describe the intensity of Mei-Yu fronts by using virtual potential temperature gradient variations [60]. The vertical cross sections of zonal mean virtual potential temperature perturbation $(\theta_v = \theta(1 + 0.61 q_v), \theta'_v = \theta_v - \overline{\theta}_v(z))$, the tendency of the virtual potential temperature gradient $(\frac{\partial}{\partial t}(\nabla \theta_v))$, and cross-front wind perturbation vectors (v', w) (here, $v' = v - V_g$) are shown in Figure 13. During the initial stage of precipitation (t = 15 h), the differences of the frontal boundaries and the cross-front circulation between the two cases are negligible. However, there is a slight difference in the intensity of the front (Figure 13a,b). Comparing the tendency of the virtual potential temperature gradients in the two cases, the difference is obvious at high levels around 6 km. While there is less of difference at low levels below 2 km. This is in agreement with the latent heat distribution.
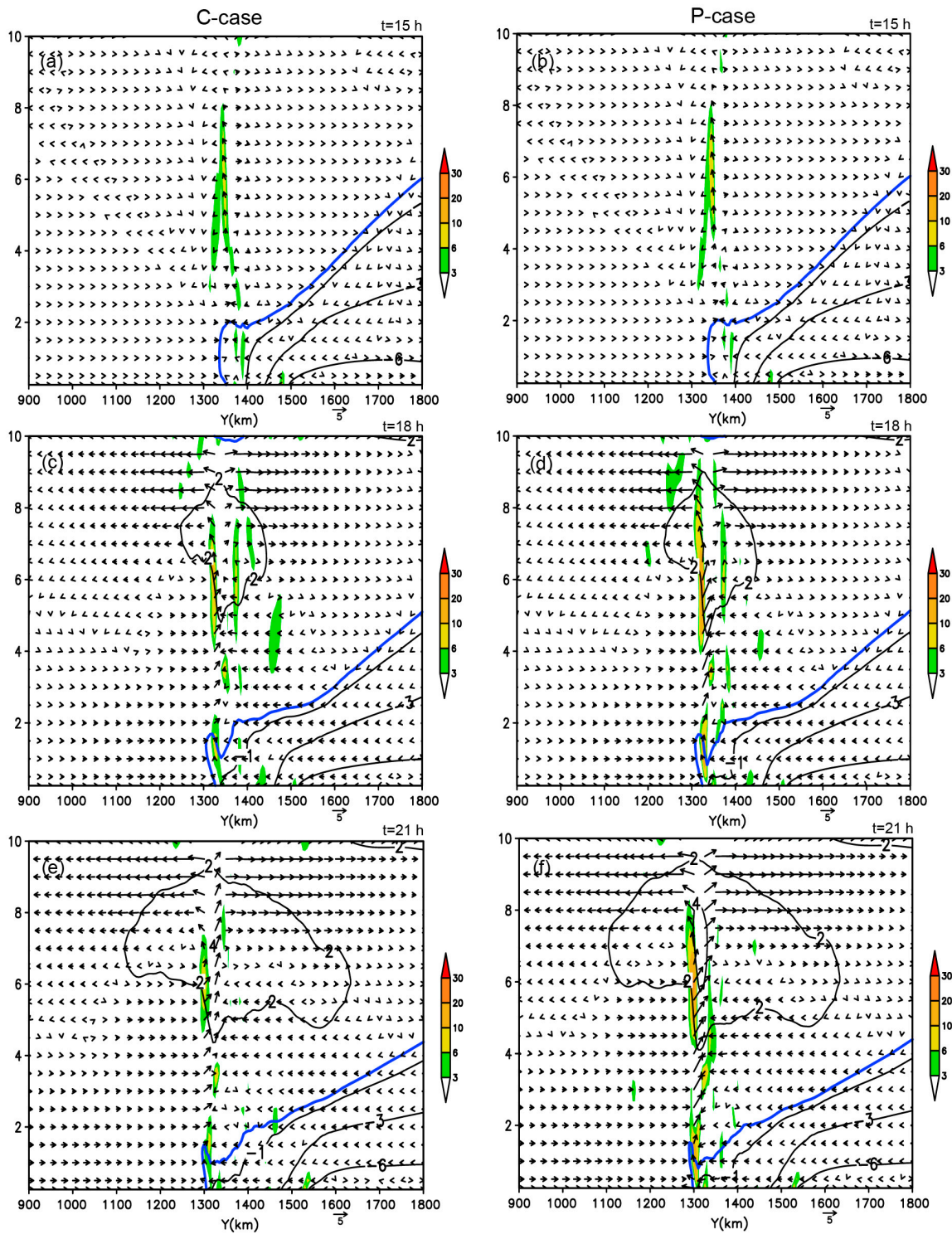
Figure 13. Vertical cross sections of zonal mean virtual potential temperature perturbation (θ'_v, 1.0 K contour interval), the tendency of the virtual potential temperature gradient (shading shows greater than 3 k/100 km · h) and cross-front wind perturbation vectors (v', w) at (**a**,**b**) t = 15 h, (**c**,**d**) 18 h and (**e**,**f**) 21 h. Negative contours are solid. The blue thick solid line highlights -0.5 K isopleth of virtual potential temperature perturbation in order to approximately delineate the leading edge of the front in the lower troposphere. Only a 900 km × 10 km of the domain is presented. The left panels show C-case, the right panels show P-case.

During the developing stage of precipitation (t = 18 h), the frontal boundaries of both cases move around 20 km to the south. Low-level convergence, high-level divergence, and cross-front ageostrophic circulation all intensify (Figure 13c,d). At this time, the greatest virtual potential temperature perturbations are above 2 K, which is at a height of 6–8 km in both cases. With development of the precipitation system, both high-level heating and low-level cooling increase further, causing the tendency of the virtual potential temperature gradient to increase at both high and low levels. In comparison, the tendencies of virtual potential temperature gradient at a height of 6 km and below 2 km enhanced significantly in P-case. It is noted that the maximum tendencies of virtual potential temperature gradient also exceeds 10 k/100 km · h at low levels. Thus, Frontogenesis associated with Mei-Yu front strengthens significantly at low levels.

At t = 21 h (Figure 13e,f), the frontal boundary in both cases moves slightly to the south. Low-level convergence, high-level divergence, and cross-front vertical circulation are all rather pronounced. By this time, the greatest virtual potential temperature perturbations have exceeded 4 K in both cases, which are still at a height of 6-8 km. The structure of the lager tendency of virtual potential temperature gradient matches with the latent heat structure (Figures 12 and 13e,f).

In comparison, the region of virtual potential temperature perturbations over 4 K was slightly larger in P-case than in C-case. The tendency of virtual potential temperature gradient is still increasing from t = 18 h to 21 h at low levels in P-case. Nevertheless, the tendency of virtual potential temperature gradient has weakened slightly by t = 21h in C-case (Figure 13c,e). This shows a continuous intensification of low-level frontogenesis in P-case. However, in C-case, low-level frontogenesis weakens, and it is much weaker than P-case.

Overall, under polluted conditions, aerosols have little effect on Mei-Yu front structure, but significantly increase the intensity of the low-level Mei-Yu front through its microphysical feedback interactions.

To explore the physical processes behind the influence of aerosols on frontogenesis, we calculate frontogenesis function [80] using the outputs from C-case and P-case numerical experiments. The expression of frontogenesis function is given by:

$$F = \frac{d}{dt} |\nabla \theta_e| = F_1 + F_2 + F_3 + F_4, \tag{14}$$

$$F_1 = -\frac{1}{2} \frac{1}{|\nabla \theta_e|} (\nabla \theta_e)^2 \cdot (\frac{\partial u}{\partial x} + \frac{\partial v}{\partial y}), \tag{15}$$

$$F_2 = -\frac{1}{2} \frac{1}{|\nabla \theta_e|} \{ [(\frac{\partial \theta_e}{\partial x})^2 - (\frac{\partial \theta_e}{\partial y})^2] \cdot (\frac{\partial u}{\partial x} - \frac{\partial v}{\partial y}) + 2(\frac{\partial \theta_e}{\partial x} \frac{\partial \theta_e}{\partial y}) \cdot (\frac{\partial v}{\partial x} + \frac{\partial u}{\partial y}) \}, \tag{16}$$

$$F_3 = -\frac{1}{|\nabla \theta_e|} \frac{\partial \theta_e}{\partial p} [\frac{\partial \theta_e}{\partial x} \frac{\partial \omega}{\partial x} + \frac{\partial \theta_e}{\partial y} \frac{\partial \omega}{\partial y}], \tag{17}$$

$$F_4 = \frac{1}{|\nabla \theta_e|} [(\nabla \theta_e \cdot \nabla) \frac{d\theta_e}{dt}]. \tag{18}$$

where *F* represents the frontogenesis function, with *F* > 0 for frontogenesis and *F* < 0 for frontolysis; F_1, F_2, F_3, and F_4 represent horizontal divergence term, horizontal deformation term, tilting term associated with vertical motion, and diabatic heating term, respectively. During the maximum precipitation period (21 h), there are three obvious frontogenesis regions at heights of 1–3 km, 4–5 km, and 10–11 km. P-case *F*-values are larger than C-case (Figure 14a,b). We primarily focus on the low-level effects. Below the height of 3 km, the frontogenesis equation is dominated by the diabatic and vertical velocity terms in both cases. The dispersion term and the horizontal deformation term also have a role. In contrast, all types of frontogenesis are larger in P-case than in C-case. Diabatic frontogenesis is mainly due to temperature gradient increases across the front. These increases are the result of the combined effects of condensation heating ahead of the front (forming a warm pool) and evaporative cooling behind

the front (forming a cool pool). This is thermal frontogenesis. The other terms in the equation are all induced by the DDE of latent heat, belonging to dynamic frontogenesis.
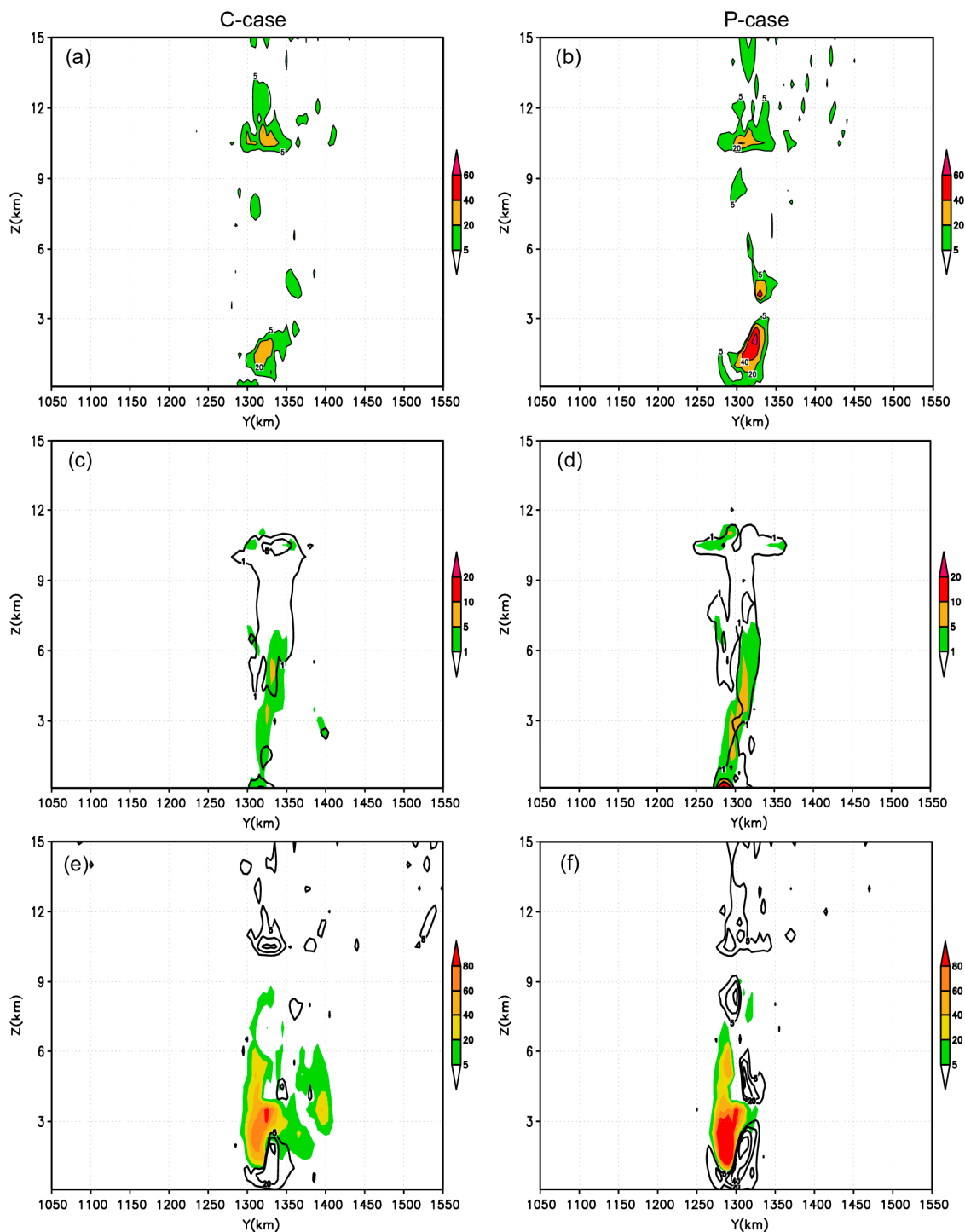

Figure 14. Vertical cross sections of zonal mean frontogenesis function at t = 21 h (Units: 1 k/100 km·h^{-1}) (**a**,**b**) F; (**c**,**d**) F_1 (shading) and F_2 (contour); (**e**,**f**) F_3 (contour) and F_4 (shading). F represents the frontogenesis function; F_1, F_2, F_3, and F_4 represent horizontal divergence term, horizontal deformation term, tilting term, and diabatic heating term, respectively. The left panels show C-case, the right panels show P-case.

High aerosol concentrations influence frontogenesis through microphysical effect and DDE. On the one hand, enhanced latent heat release (heating and cooling) produce more intense warm and

cool pools, invigorating thermal frontogenesis. On the other hand, the latent heat feedback effect strengthens updrafts ahead of the front and downdrafts behind the front, invigorating convergence near the frontal boundary and, hence, dynamic frontogenesis. Briefly, during precipitation development and maximum precipitation periods, high aerosol concentrations in Mei-Yu systems strengthen both thermal and dynamic low-level frontogenesis through microphysical feedback, leading to an intensified low-level front.

4.2.2. The Frontogenesis Effect

For frontal systems, frontogenesis can trigger ageostrophic circulation and updrafts, lifting vapor to produce clouds and precipitation. At the initial stage of cloud formation, the role of frontal circulation is significant. However, the convective system develops rapidly if it is located in both super-saturated and unstable environments. At this stage, the thermal circulation driving by latent heat dominates and overwhelms frontal circulation [42,81]. Actual circulation is the superimposition of the two (Figure 15).
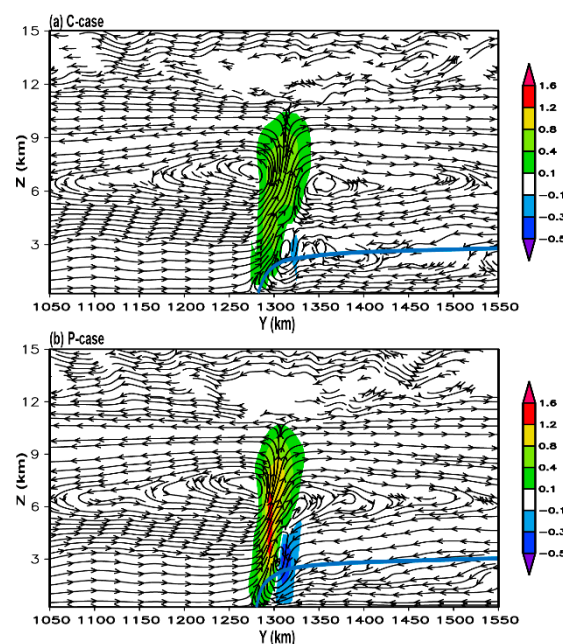

Figure 15. Vertical cross sections of zonal mean vertical velocity (w, shading) and cross-front ageostrophic circulation (v-V_g, w) at 21 h for (**a**) C-case and (**b**) P-case. Only a 500 km × 15 km of the domain is presented.

Although it is difficult to separate the two types of circulation, ageostrophic circulation generated by frontogenesis is objectively present; and stronger frontogenesis generates stronger ageostrophic circulation. Note that frontal circulation is not the same as typical thermal convective circulation. The interaction of wind shear and the cool pool at the frontal boundary separates updraft and downdraft corridors, forming tilted frontal circulation. This is similar to the slantwise convective circulation generated by wind shear and cool pools that make precipitation systems more "well-organized", strengthening intensity and prolonging its lifecycle [82]. High pollution aerosol has obvious impacts on both the thermal and dynamic fields of Mei-Yu frontal systems. As clouds and precipitation develop along the Mei-Yu front in the polluted conditions, frontogenesis is markedly intensified (Figure 15). Stronger, continuing frontogenesis benefits and maintains cross-front ageostrophic circulation (Figure 16). It also strengthens and prolongs slantwise updraft, resulting in a more "well-organized" Mei-Yu frontal system. This leads to the more sufficient interactions of the microphysical and dynamic processes influenced by aerosol and enhances precipitation. Hereinafter, "the frontogenesis effect" refers collectively to forced cross-frontal ageostrophic circulation, strengthened

and maintained slantwise updraft, and organized precipitation system. The frontogenesis effect is an indirect dynamic effect resulted from microphysical processes, latent heat release, and its DDE. In order to distinguish it from the DDE, we suggest that the indirect dynamic effect may be referred to as the second type of dynamic effect—frontogenesis dynamic effect (FDE).

4.3. Third Dynamic Effect: The Water Vapor Pump Effect

Mei-Yu front is an important part of the East Asian monsoon rainfall system, which is associated with plenty of water vapor conditions. From the above analyses, aerosol has significant influence on the dynamic field of Mei-Yu front. In addition, this rainfall system usually maintains long time, which could have important influences on the transportation of water vapor, even though very few studies have investigated the indirect vapor effect of aerosols.

Figure 16 shows the vertical cross sections of zonal mean vertical water vapor flux at t = 21 h for both cases. Maximum vertical water vapor flux in P-case is approximately double C-case. Horizontal water vapor flux is also clearly greater in P-case than C-case (Figure 17). Note that around 200 km south of the rain band, P-case horizontal water vapor flux is still 5% higher than C-case (Figure 17). This indicates that both vertical and horizontal transportation of water vapor increase significantly of Mei-Yu frontal system under polluted conditions.

From the previous sections, in polluted Mei-Yu frontal environments, both the first dynamic effect (DDE) and second dynamic effect (FDE) of aerosols can enhance low-level convergence and updrafts, which can increase low-level water vapor convergence near the front, leading to the enhanced transportation of water vapor above the frontal zone. On the other hand, in the high humidity conditions associated with the southwest monsoon, strong vertical water vapor transportation and consuming, in turn, increase the horizontal water vapor transportation in the larger-scale domain (Figure 17c). Overall, the increased updrafts and vapor transportation further enhance condensation, deposition, and collision–coalescence processes to produce more precipitable particles and to release more latent heat, which in turn can increase updrafts and further strengthen the positive feedback loop between microphysical and dynamic processes. Thus, the enhanced vapor transportation effect is driven by the first and second dynamic effects, which are rooted to latent heat release. We suggest this effect may be referred to as the third aerosol dynamic effect—vapor pump effect (VPE).

In fact, the VPE has been presented in Section 3.2 and Section 3.3, where it was pointed out that, under polluted conditions, not only freezing and deposition but also condensation is increased (Figure 10). In other words, as cold-cloud processes strengthen, warm-cloud processes also strengthen. During these processes, enhanced water vapor transportation should play an important role.

This increased water vapor transportation effect is closely related to the Mei-Yu frontal system during monsoon precipitation. Southwest flow brings plenty of water vapor to the Yangtze River Basin, forming precipitation and even long-lasting torrential rainstorms in suitable convergence conditions. Under these environments, the proper convergence near the frontal boundary can drive large-scale domain water vapor to Mei-Yu front. During the developing and mature stage of the Mei-Yu frontal precipitation system, the microphysical-thermal-dynamic coupling effect created by high concentration aerosols causes stronger updrafts, high level divergence and low-level convergence, forming the VPE. This effect enhances water vapor transportation, and further leads to more rainfall production.
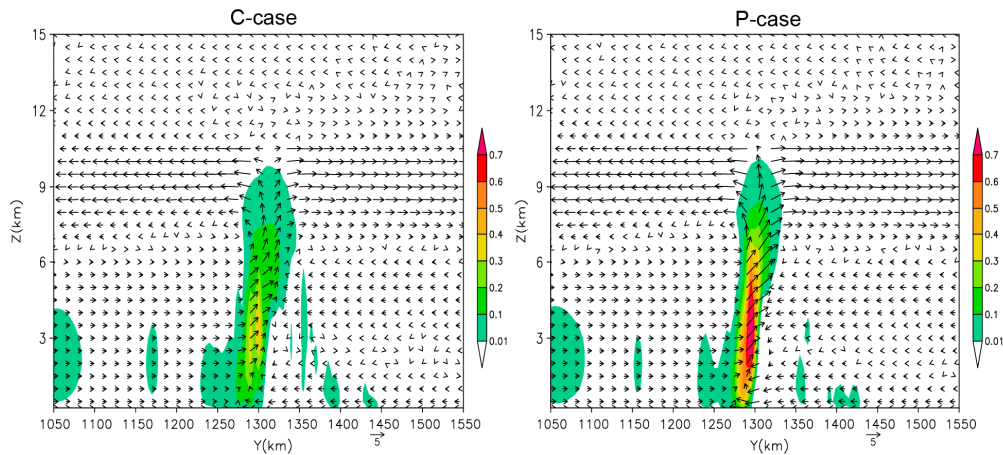
Figure 16. Vertical cross sections of zonal mean Vertical Water Vapor Flux ($|w \cdot q|/g$, shading, Units: $g \cdot cm^{-1} \cdot hPa^{-1} \cdot s^{-1}$) and cross-front wind perturbation vectors (v', w) at t = 21 h for (**a**) typical continental C-case and (**b**) polluted continental P-case. Only a 500 km × 15 km of the domain is presented.
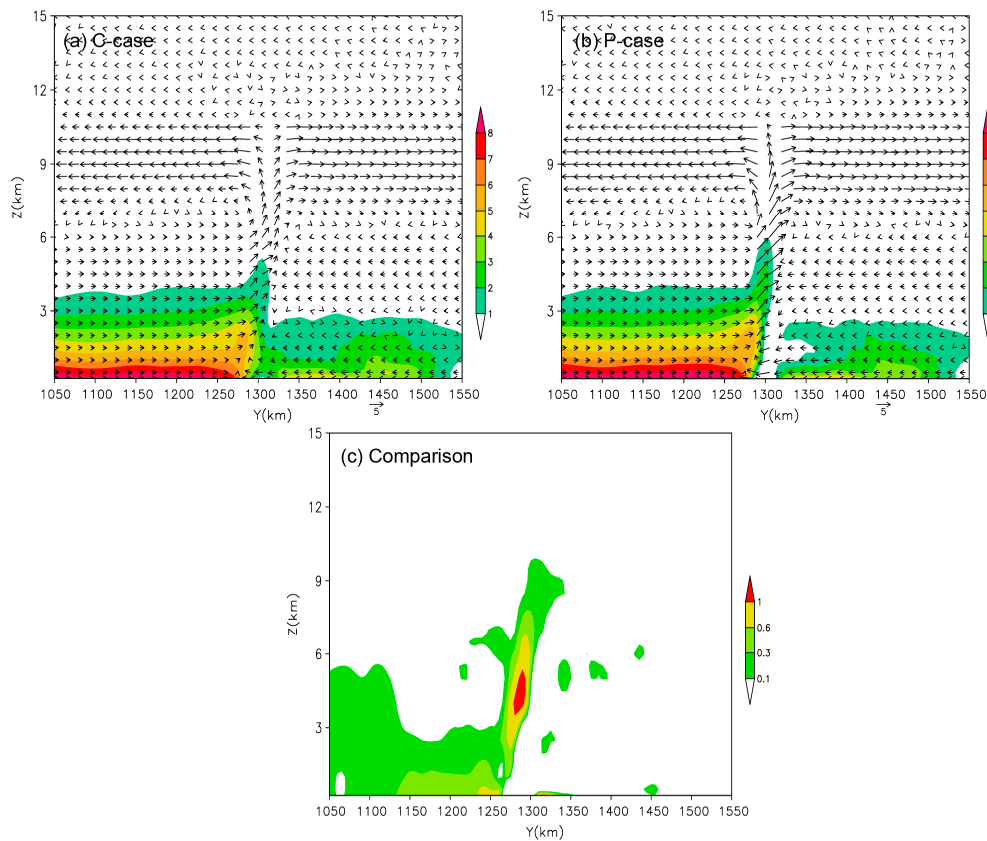

Figure 17. Vertical cross sections of zonal mean horizontal Water Vapor Flux ($V \cdot q/g$, shading, Units: $g \cdot cm^{-1} \cdot hPa^{-1} \cdot s^{-1}$) and cross-front wind perturbation vectors (v', w) at t = 21 h for (**a**) C-case and (**b**) P-case. (**c**) is the difference of horizontal Water Vapor Flux between the two cases. Only a 500 km × 15 km of the domain is presented.

5. Physical Mechanism Discussion

From the analyses of Section 3, it can be noticed that the variation of aerosol concentrations results in the differences of microphysical processes and latent heat release in Mei-Yu frontal system. The differences successively induce dynamic and water vapor variations, which in turn influence microphysical processes. These physical processes create a positive feedback loop, leading to the

increased precipitation under polluted conditions in Mei-Yu front. In general, four physical mechanisms are proposed to explain the enhancement of precipitation in Mei-Yu front. The first is the cloud microphysical mechanism, including microphysical processes and the latent heat release. The other three mechanisms are three dynamic effects resulted from the microphysical effects. They are the DDE, FDE, and VPE, respectively.

Previous studies indicated that riming increased and deposition decreased [77] or deposition enhanced and riming suppressed to produce ice phase particles under polluted conditions [37]. However, our finding shows that not only riming but also deposition enhance to produce snow and graupel in Mei-Yu frontal precipitation systems. There are two possible explanations for the enhanced deposition. First, WBF process is enhanced, because more cloud droplets are transported above the 0 °C isotherm where they may evaporate and deposited onto ice-phase particles. Second, the increased cold-cloud processes enhance latent heat release, leading to stronger updrafts and transportation of water vapor to high levels to strengthen deposition. On the other hand, the increased deposition releases more latent heat and increases updrafts that enhance riming process. The mutual promotion of riming and deposition increases the growth of snow and graupel in the strong updraft region and then increases cold-rain process.

During the developing and maximum precipitation stages of Mei-Yu front system, the enhanced melting and evaporation can strengthen dynamic processes at the low-level frontal boundary, and drive and strengthen warm-cloud processes (condensation and collision-coalescence). Likewise, strengthened warm-cloud processes release more condensation heating, strengthening updrafts, which in turn promotes cold-cloud processes. Thus, with the cold-cloud "towing" effect, there is mutual promotion of cold and warm-cloud processes. This could be an even more complicated and peculiar cloud microphysical mechanism of aerosol effects on Mei-Yu front precipitation.

Regarding latent heat release, previous researchers emphasized that increased high-level freezing heating was the major difference under polluted conditions [25,77]. Our research shows that in polluted Mei-Yu frontal cloud systems, high-level heating due to both freezing and deposition processes increases, but deposition heating is much greater than freezing heating. In addition, due to the increased high-level cold-cloud heating, there is increased updraft that not only increases collision-coalescence processes, but also greatly increased vertical transportation of water vapor because of the high humidity environment of Mei-Yu fronts. This leads to deposition and condensation processes all increasing as well (Figure 10). Furthermore, deposition and condensation processes cause much greater heating than freezing. Because of this, the key mechanism behind increased heating is increased deposition and the condensation processes with the cold-cloud "towing". On the other hand, previous studies pointed that low-level evaporative cooling had a key impact on low-level convergence [30]. Our studies indicated that evaporative cooling is the main driver of low-level convergence, and melting cooling also plays a role (Figures 11 and 12).

Regarding dynamic effects, the similarities between the previous results of convective systems [25,30,34,77,78] and our findings of Mei-Yu front are that increased heating strengthens updrafts, and increased cooling strengthens downdrafts, which in turn strengthens low-level convergence. However, there are also some differences and new insights in our findings. We refer to the stronger updrafts (due to the latent heat–dynamic effect) and convergence (due to the cool pool effect) pointed out by Tao et al. [78] as DDE, which has a very significant effect on the precipitation enhancement in convective clouds and mixed clouds. However, in Mei-Yu system, in addition to DDE, FDE is also an important mechanism for the precipitation enhancement under polluted conditions. Under the role of the frontal vertical wind shear, FDE forces ageostrophic circulation and forms slantwise convective circulation patterns (updrafts and downdrafts are separated) which contributes to strengthening and maintaining updrafts, causing a more "well-organized" Mei-Yu frontal system. And this further strengthens and prolongs precipitation.

Regarding the VPE, Khain et al. [25] mentioned that increased squall line precipitation maybe related to the gathering of water vapor from a larger region into a smaller region, but they did not

analyze further. This paper presents a "water vapor pump" effect in Mei-Yu front caused by aerosols in positive feedback loops. It is particularly pointed out that Mei-Yu front is monsoon precipitation system. With the large-scale sufficient water vapor conditions, deep frontal clouds, and long-time precipitation, the long-lasting water vapor convergence and vertical transportation can tow and drive large-scale domain water vapor to Mei-Yu front. The enhanced water vapor transportation effect, in turn, strengthens condensation, deposition and even collision–coalescence processes, leading to more latent heat release, which further enhance the "microphysical–dynamic feedback loop". Note that this effect has not been reported in the previous studies yet.

The four physical mechanisms resulted from high aerosol concentrations in Mei-Yu frontal systems have different influences in different stage of precipitation. The first mechanism, the microphysical mechanism, affects the entire precipitation process. Especially, the microphysical effects on precipitation dominate the early stages of precipitation. With the precipitation development, the other three dynamic effects gradually become active. Among them, DDE is the most direct. FDE are driven by latent heat release and DDE in Mei-Yu frontal environments. The increasing and maintaining low-level frontogenesis can strengthen the intensity of the original front and play an important role in strengthening and prolonging the precipitation. That is to say, FDE only in the frontal precipitation system is more significant. Furthermore, VPE becomes obvious only in Mei-Yu front associated with monsoon systems. It may not be obvious in short-lived isolated convection systems.
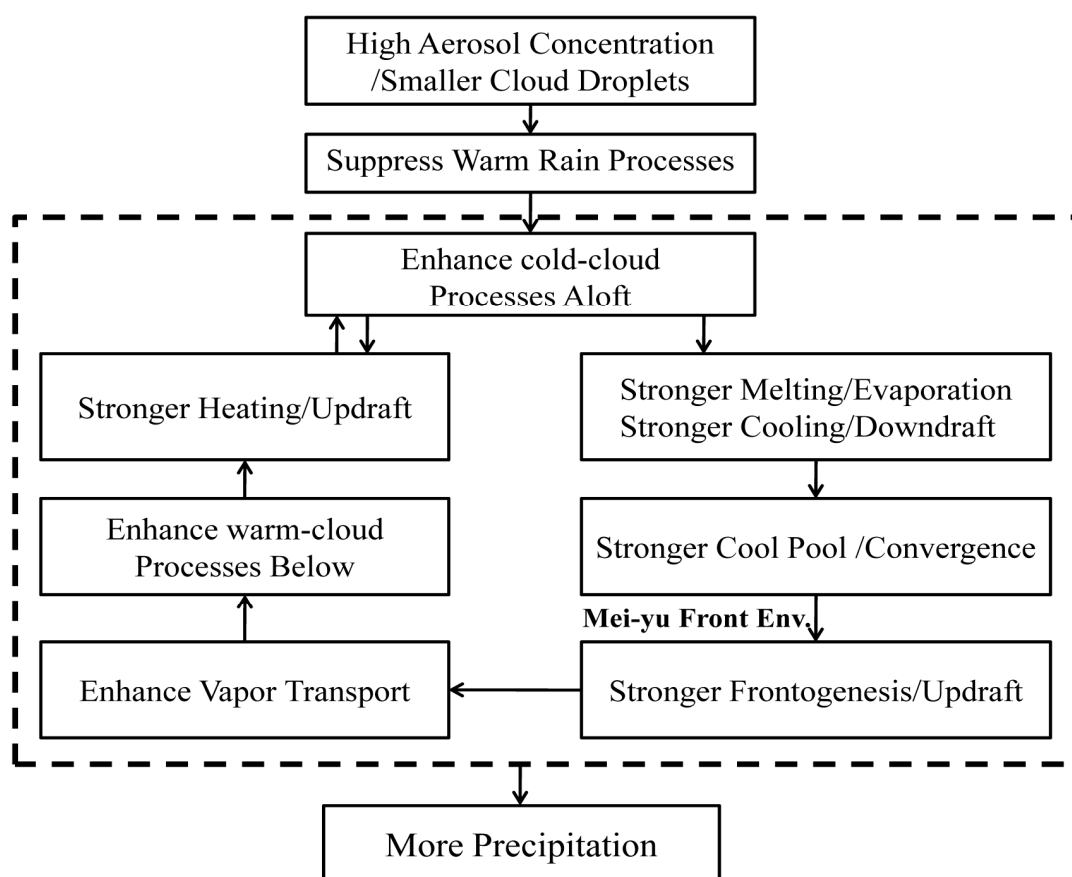

Figure 18. Schematic diagram showing the main physical processes by which aerosols affect Mei-Yu precipitation in the polluted continental environment.

The aerosol impacts on Mei-Yu frontal clouds and precipitation are summarized in a schematic diagram (Figure 18). The figure describes the main physical processes through which high aerosol concentration affects Mei-Yu frontal clouds and precipitation via four mechanisms. High aerosol concentrations first influence cloud microphysical processes and their accompanying latent heat

release. Increased updrafts, downdrafts, and low-level convergence create the direct dynamic effect. The direct dynamic effect re-invigorates the cloud microphysical processes that create it, forming the first positive feedback loop. In Mei-Yu frontal system, the cool pool effect and direct dynamic effect caused by microphysical processes result in frontogenesis which increases frontal dynamic processes and strengthens the slantwise updrafts, thereby forming the VPE. Increased water vapor transportation in turn strengthens microphysical processes. Thus, these processes form the second positive feedback loop.

The interaction of several physical processes form and strengthen the two types of "microphysical–dynamic positive feedback loop", leading to the more "well-organized" Mei-Yu front system and enhanced precipitation. The interaction of microphysical processes and frontal dynamic processes, and the two positive feedback loops they create, are the major mechanisms by which aerosols affect Mei-Yu frontal precipitation.

6. Summary and Conclusions

In this study, the impact of polluted (P-case) conditions versus typical (C-case) continent conditions on an ideal Mei-Yu front was simulated via WRF coupled with a bulk two-moment microphysics scheme [63]. The primary focus was on exploring physical mechanisms of simulated aerosol effects in the face of complex process interactions and feedbacks between the cloud microphysics and dynamics in Mei-Yu frontal system. We summarized three dynamic effects resulted from the microphysical mechanisms and revealed two microphysical/dynamic positive feedback loops in polluted Mei-Yu frontal environments. The main conclusions are as follows:

(1) Aerosols play an important role in affecting local precipitation around Mei-Yu fronts. Polluted conditions delay the onset of precipitation but strengthen precipitation during the intense precipitation period and increase the amount of total precipitation. This may be one of the reasons for the increased frequency of the intense Mei-Yu precipitation in recent years. Note that anthropogenic pollution has a significant effect on Mei-Yu front precipitation. This may be an important feature influencing climate change in East Asia.

(2) Aerosols affect Mei-Yu frontal precipitation by first changing microphysical processes. Under polluted conditions, these more numerous and smaller cloud droplets suppressed auto-conversion and collision–coalescence processes, and hence resulted in late raindrop formation, which initially delays the onset of Mei-Yu precipitation. However, a larger amount of cloud water is transported to above the freezing level, increasing ice-phase particle growth by riming and the WBF processes, and producing large amounts of snow and graupel. The melting of snow and graupel is the main reason why rain increases. Furthermore, during the developing and mature stages, cold rain processes are more vigorous under polluted conditions. With cold-cloud processes "towing", warm-cloud progresses are encouraged. Thus, cold-cloud and warm-cloud interactions mutually boost each other. This is perhaps the more complicated and particular microphysical mechanism by which aerosols affects Mei-Yu frontal precipitation.

(3) High aerosol concentrations first influence cloud microphysical processes, enhance latent heat release, and then strengthen updrafts, downdrafts, and low-level convergence, forming DDE. In turn, DDE further strengthens microphysical processes and creates the first positive feedback loop. In Mei-Yu frontal environments, the enhanced DDE and the cool pool effect result in stronger frontogenesis, which strengthens frontal dynamic processes. This further increases both vertical and horizontal transportation of water vapor and form VPE, which in turn strengthens microphysical processes and creates the second positive feedback loop. Many physical processes and effects interact with each other, forming and strengthening both microphysical–dynamic feedback loops, leading to the well-organized Mei-Yu front precipitation system. Overall, the combined effect is to increase Mei-Yu front precipitation. The interaction of microphysical processes and dynamic processes, and the positive feedback loops they create, are the main physical mechanisms behind the impacts of aerosol on Mei-Yu frontal precipitation.

Notably, a series of ideal frontal experiments are carried out herein by using a domain-averaged initial sounding of a typical Mei-Yu system. The results could represent the typical Mei-Yu frontal systems, but not all of Mei-Yu frontal temperatures and humidity. On the other hand, the cloud physics scheme used in this paper simplifies the cloud–aerosol interactions by setting cloud droplet concentrations to reflect changes in aerosol concentration. In addition, it does not consider the impacts of aerosols on ice nuclei. The above simplifications may affect the accuracy of our conclusions about the impacts of aerosols on the magnitude of precipitation. This paper investigated the overall impacts of increased aerosols on Mei-Yu front precipitation in highly polluted regions, such as the Yangtze River Basin in China. In reality, Mei-Yu fronts can extend from interior of southern China to southern Japan over varying geography and pollution conditions. The impacts of local atmospheric pollution on the entire Mei-Yu rainband will be investigated in future work.

Author Contributions: Conceptualization, Y.Z. and Z.W.; Methodology, Z.W.; Software, L.Z.; Validation, Z.W., Y.Z. and L.Z.; Formal analysis, Z.W.; Investigation, H.Z.; Resources, Y.Z.; Data curation, H.L.; Writing—original draft preparation, Z.W.; Writing—review and editing, X.M.; Visualization, Y.X.; Supervision, Y.Z.; Project administration, L.Z.; Funding acquisition, L.Z.

Conflicts of Interest: The authors declare no conflict of interest.

References

1. Xu, X.; Ren, W. Prediction of Air Pollution Concentration Based on mRMR and Echo State Network. *Appl. Sci.* **2019**, *9*, 1811. [CrossRef]
2. Błaszczak, B.; Widziewicz-Rzońca, K.; Zioła, N.; Klejnowski, K.; Juda-Rezler, K. Chemical Characteristics of Fine Particulate Matter in Poland in Relation with Data from Selected Rural and Urban Background Stations in Europe. *Appl. Sci.* **2019**, *9*, 98. [CrossRef]
3. Guo, J.J.; Zhang, X.X.; Wu, Y.Y.; Zhaxi, Y.; Che, H.Z.; La, B.; Wang, W.; Li, X.W. Spatio-temporal variation trends of satellite-based aerosol optical depth in China during 1980–2008. *Atmos. Environ.* **2011**, *45*, 6802–6811. [CrossRef]
4. Chen, T.; Guo, J.; Li, Z.; Zhao, C.; Liu, H.; Cribb, M.; Wang, F.; He, J. A CloudSat perspective on the cloud climatology and its association with aerosol perturbations in the vertical over eastern China. *J. Atmos. Sci.* **2016**, *73*, 3599–3616. [CrossRef]
5. Huo, F.; Ma, H.; Song, J.; Dai, A.; Jiang, Z. Impact of Chinese Urbanization and Aerosol Emissions on the East Asian Summer Monsoon. *J. Clim.* **2017**, *30*, 1019–1039.
6. Li, Z.; Niu, F.; Fan, J.; Liu, Y.; Rosenfeld, D.; Ding, Y. Long-term impacts of aerosols on the vertical development of clouds and precipitation. *Nat. Geosci.* **2011**, *4*, 888–894. [CrossRef]
7. Xin, J.; Wang, Y.; Pan, Y.; Ji, D.; Liu, Z.; Wen, T.; Wang, Y.; Li, X.; Sun, Y.; Sun, J.; et al. The Campaign on Atmospheric Aerosol Research Network of China: CARE-China. *Bull. Am. Meteorol. Soc.* **2015**, *96*, 1137–1155. [CrossRef]
8. Braun, R.A.; Dadashazar, H.; Macdonald, A.B.; Aldhaif, A.M.; Maudlin, L.C.; Crosbie, E.; Aghdam, M.A.; Mardi, A.H.; Sorooshian, A. Impact of Wildfire Emissions on Chloride and Bromide Depletion in Marine Aerosol Particles. *Environ. Sci. Technol.* **2017**, *51*, 9013–9021. [CrossRef]
9. Li, Z.Q.; Xu, H.; Li, K.T.; Li, D.H.; Xie, Y.S.; Li, L.; Zhang, Y.; Gu, X.F.; Zhao, W.; Tian, Q.J.; et al. Comprehensive Study of Optical, Physical, Chemical, and Radiative Properties of Total Columnar Atmospheric Aerosols over China: An Overview of Sun–Sky Radiometer Observation Network (SONET) Measurements. *Bull. Am. Meteorol. Soc.* **2018**, *99*, 739–755. [CrossRef]
10. Sorooshian, A.; Anderson, B.; Bauer, S.E.; Braun, R.A.; Cairns, B.; Crosbie, E.; Dadashazar, H.; Diskin, G.; Ferrare, R.; Flagan, R.C.; et al. Aerosol–Cloud–Meteorology Interaction Airborne Field Investigations: Using Lessons Learned from the U.S. West Coast in the Design of ACTIVATE off the U.S. East Coast. *Bull. Am. Meteorol. Soc.* **2019**, *100*, 1511–1528. [CrossRef]
11. Liu, Q.; Quan, J.; Jia, X.; Sun, Z.; Li, X.; Gao, Y.; Liu, Y. Vertical Profiles of Aerosol Composition over Beijing, China: Analysis of in Situ Aircraft Measurements. *J. Atmos. Sci.* **2019**, *76*, 231–245. [CrossRef]

12. Niu, F.; Li, Z. Systematic variations of cloud top temperature and precipitation rate with aerosols over the global tropics. *Atmos. Chem. Phys.* **2012**, *12*, 8491–8498. [CrossRef]

13. Wang, F.; Guo, J.; Wu, Y.; Zhang, X.; Deng, M.; Li, X.; Zhang, J.; Zhao, J. Satellite observed aerosol-induced variability in warm cloud properties under different meteorological conditions over eastern China. *Atmos. Environ.* **2014**, *84*, 122–132. [CrossRef]

14. Peng, J.; Li, Z.; Zhang, H.; Liu, J.; Cribb, M. Systematic Changes in Cloud Radiative Forcing with Aerosol Loading for Deep Clouds in the Tropics. *J. Atmos. Sci.* **2016**, *73*, 231–249. [CrossRef]

15. Ackerman, S.A.; Platnick, S.; Bhartia, P.K.; Duncan, B.; L'Ecuyer, T.; Heidinger, A.; Skofronick-Jackson, G.; Loeb, N.; Schmit, T.; Smith, N. Satellites See the World's Atmosphere. *Meteorol. Monogr.* **2018**, *59*, 4.1–4.53. [CrossRef]

16. Lohmann, U. A glaciation indirect effect caused by soot aerosols. *Geophys. Res. Lett.* **2002**. [CrossRef]

17. Rosenfeld, D. Suppression of rain and snow by urban and industrial air pollution. *Science* **2000**, *287*, 1793–1796. [CrossRef] [PubMed]

18. Khain, A.; Pokrovsky, A.; Pinsky, M.; Seigert, A.; Phillips, V. Simulation of effects of atmospheric aerosols on deep turbulent convective clouds using a spectral microphysics mixed-phase cumulus cloud model. Part I: Model description and possible applications. *J. Atmos. Sci.* **2004**, *61*, 2983–3001. [CrossRef]

19. Khain, A.; Pokrovsky, A. Simulation of effects of atmospheric aerosols on deep turbulent convective clouds using a spectral microphysics mixed-phase cumulus cloud model. Part II: Sensitivity study. *J. Atmos. Sci.* **2004**, *61*, 2963–2982. [CrossRef]

20. Givati, A.; Rosenfeld, D. Quantifying Precipitation Suppression Due to Air Pollution. *J. Appl. Meteorol.* **2004**, *43*, 1038–1056. [CrossRef]

21. Borys, R.D.; Lowenthal, D.H.; Cohn, S.A.; Brown, W.O.J. Mountaintop and radar measurements of anthropogenic aerosol effects on snow growth and snowfall rate. *Geophys. Res. Lett.* **2003**, *30*, 1538. [CrossRef]

22. Duan, J.; Mao, J. Progress in Researches on Interaction between Aerosol and Cloud. *Adv. Earth Sci.* **2008**, *23*, 252–261.

23. Xiao, H.; Yin, Y. A Numerical Study of Polluted Aerosol Effects on Precipitation in Shanxi Province. *Chin. J. Atmos. Sci.* **2011**, *35*, 235–246.

24. Rosenfeld, D.; Woodley, W.L. Deep convective clouds with sustained supercooled liquid water down to—37.5 °C. *Nature* **2000**, *405*, 440–442. [CrossRef] [PubMed]

25. Khain, A.; Rosenfeld, D.; Pokrovsky, A. Aerosol impact on the dynamics and microphysics of deep convective clouds. *Q. J. R. Meteorol. Soc.* **2005**, *131*, 2639–2663. [CrossRef]

26. Fan, J.; Zhang, R.; Li, G.; Tao, W.-K. Effects of aerosols and relative humidity on cumulus clouds. *J. Geophys. Res.* **2007**, *112*, 14204. [CrossRef]

27. Lin, J.C.; Matsui, T.; Pielke, R.A.; Kummerow, C. Effects of biomass-burning-derived aerosols on precipitation and clouds in the Amazon Basin: A satellite-based empirical study. *J. Geophys. Res.* **2006**, *111*, 19204. [CrossRef]

28. Heever, S.C.V.D.; Carrió, G.G.; Cotton, W.R.; DeMott, P.J.; Prenni, A.J. Impact of nucleating aerosol on Florida storms, Part 1: Mesoscale simulations. *J. Atmos. Sci.* **2006**, *63*, 1752–1775. [CrossRef]

29. Zhang, H.; McFarquhar, G.M.; Saleeby, S.M.; Cotton, W.R. Impacts of Saharan dust as CCN on the evolution of an idealized tropical cyclone. *Geophys. Res. Lett.* **2007**, *34*, 14812. [CrossRef]

30. Tao, W.-K.; Li, X.; Khain, A.; Matsui, T.; Lang, S.; Simpson, J. Role of atmospheric aerosol concentration on deep convective precipitation: Cloud-resolving model simulations. *J. Geophys. Res.* **2007**, *112*. [CrossRef]

31. Lynn, B.H.; Khain, A.; Dudhia, J.; Rosenfeld, D.; Rovsky, A.P.; Seifert, A. Spectral (bin) microphysics coupled with a mesoscale model (MM5) Part II: Simulation of a CAPE rain event with a squall line. *Mon. Weather Rev.* **2005**, *133*, 59–71. [CrossRef]

32. Seifert, A.; Beheng, K.D. A two-moment cloud microphysics parameterization for mixed-phase clouds. Part 2: Maritime vs. continental deep convective storms. *Meteorol. Atmos. Phys.* **2006**, *92*, 67–82. [CrossRef]

33. Cotton, W.R.; Zhang, H.; McFarquhar, G.M.; Saleeby, S.M. Should we consider polluting hurricanes to reduce their intensity. *J. Weather Modif.* **2007**, *39*, 70–73.

34. Khain, A.; Lynn, B.; Dudhia, A.J. Aerosol Effects on Intensity of Landfalling Hurricanes as Seen from Simulations with the WRF Model with Spectral Bin Microphysics. *J. Atmos. Sci.* **2010**, *67*, 365–384. [CrossRef]

35. Rosenfeld, D.; Woodley, W.L.; Khain, A.; Cotton, W.R.; Carrió, G.; Ginis, I.; Golden, J.H. Aerosol Effects on Microstructure and Intensity of Tropical Cyclones. *Bull. Am. Meteorol. Soc.* **2012**, *93*, 987–1001. [CrossRef]

36. Jiang, B.; Huang, B.; Lin, W.; Xu, S. Investigation of the Effects of Anthropogenic Pollution on Typhoon Precipitation and Microphysical Processes Using WRF-Chem. *J. Atmos. Sci.* **2016**, *73*, 1593–1610. [CrossRef]

37. Saleeby, S.M.; Posselt, D.J.; Igel, A.L.; Heever, S.C.V.D.; Naud, C.M. Sensitivity of Warm-Frontal Processes to Cloud-Nucleating Aerosol Concentrations. *J. Atmos. Sci.* **2013**, *70*, 1768–1783.

38. Thompson, G.; Eidhammer, T. A Study of Aerosol Impacts on Clouds and Precipitation Development in a Large Winter Cyclone. *J. Atmos. Sci.* **2014**, *71*, 3636–3658. [CrossRef]

39. Sampe, T.; Xie, S.P. Large-Scale Dynamics of the Meiyu-Baiu Rainband: Environmental Forcing by the Westerly Jet. *J. Clim.* **2010**, *23*, 113–134. [CrossRef]

40. Kuwano-Yoshida, A.; Taguchi, B.; Xie, S.P. Baiu Rainband Termination in Atmospheric and Coupled Atmosphere–Ocean Models. *J. Clim.* **2013**, *26*, 10111–10124. [CrossRef]

41. Ninomiya, K.; Akiyama, T. Multi-scale Features of Baiu, the Summer Monsoon over Japan and the East Asia. *J. Meteorol. Soc. Jpn.* **1992**, *70*, 467–495. [CrossRef]

42. Yoshizaki, M.; Kato, T.; Tanaka, Y.; Takayama, H.; Shoji, Y.; Seko, H.; Arao, K.; Manabe, K.; Members of X-BAIU-98 Observation. Analytical and Numerical Study of the 26 June 1998 Orographic Rainband Observed in Western Kyushu, Japan. *J. Meteorol. Soc. Jpn.* **2000**, *78*, 835–856. [CrossRef]

43. Ding, Y.H.; Chan, J.C.L. The East Asian summer monsoon: An overview. *Meteorol. Atmos. Phys.* **2005**, *89*, 117–142.

44. Xu, Q. Recent strong decadal change of Mei-yu in 121 years. *Adv. Water Sci.* **2007**, *18*, 327–335.

45. Zhang, D.-E. A Study of the Large Scale Flooding over Eastern China in 1755. *Adv. Clim. Chang. Res.* **2012**, *3*, 128–137. [CrossRef]

46. Ma, Y.; Chen, W.; Wang, L. A comparative study of the interannual variation of summer rain-fall anomalies between the Huaihe Mei-yu season and the Jiangnan Meiyu season and their climate background. *Acta Meteorol. Sin.* **2011**, *69*, 334–343.

47. Wu, Z.; Zhang, Y.; Zhang, L.; Hao, X.; Lei, H.; Zheng, H. Validation of GPM Precipitation Products by Comparison with Ground-Based Parsivel Disdrometers over Jianghuai Region. *Water* **2019**, *11*, 1260. [CrossRef]

48. Sun, Y.; Yin, D.P.; Yao, L.N.; Cao, S.Y. Temporal and spatial distribution and circulation features of the Mei-yu precipitation anomaly in Jiangsu in the latest 50 years. *Torrential Rain Disasters* **2012**, *31*, 149–154.

49. Huang, W.; Yu, R.C.; Li, J. Analysis of changes in precipitation intensity in later-summer over southeast coast of china in 1967–2006. *Adv. Clim. Chang. Res.* **2012**, *8*, 164–170.

50. Duan, J.; Mao, J.T. Study on the distribution and variation trends of atmospheric aerosol optical depth over the Yangtze River Delta. *Acta Sci. Circumst.* **2007**, *27*, 537–543.

51. Yu, X.; Zhu, B.; Yin, Y.; Fan, S.; Chen, A. Seasonal variation of columnar aerosol optical properties in Yangtze River Delta in China. *Adv. Atmos. Sci.* **2011**, *28*, 1326–1335. [CrossRef]

52. Luo, Y.X.; Chen, J.; Zheng, X.B.; Zhao, T.L. Climatology of aerosol optical depth over China from recent 10 years of MODIS remote sensing data. *Ecol. Environ. Sci.* **2012**, *21*, 876–883. [CrossRef]

53. Yu, X.; Ma, J.; Kumar, K.R.; Zhu, B.; An, J.; He, J.; Li, M. Measurement and analysis of surface aerosol optical properties over urban Nanjing in the Chinese Yangtze River Delta. *Sci. Total Environ.* **2016**, *542*, 277–291. [CrossRef] [PubMed]

54. Zhuang, B.; Wang, T.; Liu, J.; Li, S.; Xie, M.; Han, Y.; Chen, P.; Hu, Q.; Yang, X.Q.; Fu, C.; et al. The surface aerosol optical properties in the urban area of Nanjing, west Yangtze River Delta, China. *Atmos. Chem. Phys.* **2017**, *17*, 1143–1160. [CrossRef]

55. Qin, Y.S.; Yin, Y.; Yang, S.Y.; Chen, K. Chemical characteristics of the aerosols and their effect on microphysical properties of clouds in spring and summer over Mt. Huang. *Acta Meteorol. Sin.* **2012**, *70*, 1334–1346.

56. Yin, Y.; Chen, Q.; Jin, L.; Chen, B.; Zhu, S.; Zhang, X. The effects of deep convection on the concentration and size distribution of aerosol particles within the upper troposphere: A case study. *J. Geophys. Res. Atmos.* **2012**, *117*, D22. [CrossRef]

57. Yue, Y.; Niu, S.; Sang, J.; lÜ, J. Observational study on the distribution of cloud condensation nuclei and its causes in drought region. *China Environ. Sci.* **2010**, *30*, 593–598.

58. Ke, S.; Yu, W.; Cao, J.; Wang, T. Aerodynamic Force and Comprehensive Mechanical Performance of a Large Wind Turbine during a Typhoon Based on WRF/CFD Nesting. *Appl. Sci.* **2018**, *8*, 1982. [CrossRef]

59. Skamarock, W.C.; Klemp, J.B.; Dudhia, J.; Gill, D.O.; Barker, D.M.; Duda, M.; Huang, X.-Y.; Wang, W.; Powers, J.G. A description of the advanced research WRF version 3. NCAR Tech. Note TN-475+STR. *Cent. Atmos. Res.* **2008**. [CrossRef]

60. Peng, J.; Zhang, L.; Luo, Y.; Zhang, Y. Mesoscale Energy Spectra of the Mei-Yu Front System. Part I: Kinetic Energy Spectra. *J. Atmos. Sci.* **2014**, *71*, 37–55. [CrossRef]

61. Klemp, J.B.; Dudhia, J.; Hassiotis, A.D. An upper gravity-wave absorbing layer for NWP applications. *Mon. Weather Rev.* **2008**, *136*, 3987–4004. [CrossRef]

62. Morrison, H. On the robustness of aerosol effects on an idealized super cell storm simulated with a cloud system-resolving model. *Atmos. Chem. Phys.* **2012**, *12*, 7689–7705. [CrossRef]

63. Morrison, H.; Thompson, G.; Tatarskii, V. Impact of cloud microphysics on the development 20 of trailing stratiform precipitation in a simulated squall line: Comparison of one and two moment schemes. *Mon. Weather Rev.* **2009**, *137*, 991–1007. [CrossRef]

64. Twomey, S. The influence of pollution on the shortwave albedo of clouds. *J. Atmos. Sci.* **1977**, *34*, 1149–1152. [CrossRef]

65. Khain, A.; Lynn, B. Simulation of a supercell storm in clean and dirty atmosphere using weather research and forecast model with spectral bin microphysics. *J. Geophys. Res. Atmos.* **2009**, *114*, D19. [CrossRef]

66. Lim, K.-S.S.; Hong, S.-Y.; Yum, S.S.; Dudhia, J.; Klemp, J.B. Aerosol effects on the development of a supercell storm in a double-moment bulk-cloud microphysics scheme. *J. Geophys. Res. Space Phys.* **2011**, *116*. [CrossRef]

67. Simpson, J.; Woodley, W.L. Seeding Cumulus in Florida: New 1970 Results. *Science* **1971**, *172*, 117–126. [CrossRef]

68. Cotton, W.R. Cloud physics: A review for 1975–1978 IUGG Quadrennial Report. *Rev. Geophys.* **1979**, *17*, 1840–1851. [CrossRef]

69. Andreae, M.O.; Rosenfeld, D.; Artaxo, P.; Costa, A.A.; Frank, G.P.; Longo, K.M.; Silva-Dias, M.A.F. Smoking rain clouds over the Amazon. *Science* **2004**, *303*, 1337–1341. [CrossRef]

70. Wang, Z.; Wang, T.; Guo, J.; Gao, R.; Xue, L.; Zhang, J.; Zhou, Y.; Zhou, X.; Zhang, Q.; Wang, W. Formation of secondary organic carbon and cloud impact on carbonaceous aerosols at Mount Tai, North China. *Atmos. Environ.* **2012**, *46*, 516–527. [CrossRef]

71. Xia, X.; Li, Z.; Holben, B.; Wang, P.; Eck, T.; Chen, H.; Cribb, M.; Zhao, Y. Aerosol optical properties and radiative effects in the Yangtze Delta region of China. *J. Geophys. Res. Space Phys.* **2007**, *112*. [CrossRef]

72. Dong, H.; Xu, H.M.; Luo, Y.L. Effects of Cloud Condensation Nuclei Concentration on Precipitation in Convection Permitting Simulations of a Squall Line Using WRF Model: Sensitivity to Cloud Microphysical Schemes. *Chin. J. Atmos. Sci.* **2012**, *36*, 145–169.

73. Kawashima, M. Numerical Study of Precipitation Core-Gap Structure along Cold Fronts. *J. Atmos. Sci.* **2007**, *64*, 2355–2377. [CrossRef]

74. Wang, P.; Yang, J. Observation and Numerical Simulation of Cloud Physical Processes Associated with Torrential Rain of the Meiyu Front. *Adv. Atmos. Sci.* **2003**, *20*, 77–96. [CrossRef]

75. Zhang, Y.; Lei, H.; Pan, X.; Wang, C.; Xie, Y. Study on cloud micro-physical processes and precipitation formative mechanisms of a mesoscale convective system in Meiyu front in June 2004. *Sci. Meteorol. Sin.* **2009**, *29*, 434–446.

76. Morrison, H.; Pinto, J.O. Mesoscale Modeling of Springtime Arctic Mixed-Phase Stratiform Clouds Using a New Two-Moment Bulk Microphysics Scheme. *J. Atmos. Sci.* **2005**, *62*, 3683–3704. [CrossRef]

77. Han, J.-Y.; Baik, J.-J.; Khain, A. A Numerical Study of Urban Aerosol Impacts on Clouds and Precipitation. *J. Atmos. Sci.* **2012**, *69*, 504–520. [CrossRef]

78. Tao, W.-K.; Chen, J.-P.; Li, Z.; Wang, C.; Zhang, C. Impact of Aerosols on Convective Clouds and Precipitation. *Rev. Geophys.* **2012**, *50*, 1–62. [CrossRef]

79. Cheng, C.-T.; Wang, W.-C.; Chen, J.-P. Simulation of the effects of increasing cloud condensation nuclei on mixed-phase clouds and precipitation of a front system. *Atmos. Res.* **2010**, *96*, 461–476. [CrossRef]

80. Ninomiya, K. Characteristics of Baiu Front as a Predominant Subtropical Front in the Summer Northern Hemisphere. *J. Meteorol. Soc. Jpn.* **1984**, *62*, 880–894. [CrossRef]

81.　Ross, B.B.; Orlanski, I. The Circulation Associated with a Cold Front. Part II: Moist Case. *J. Atmos. Sci.* **1978**, *35*, 445–465. [CrossRef]

82.　Rotunno, R.; Klemp, J.B.; Weisman, M.L. A theory for strong, long-lived squall lines. *J. Atmos. Sci.* **1988**, *45*, 463–485. [CrossRef]